J. Fluid Mech. (2010), *vol.* 656, *pp.* 231–259.
doi:10.1017/S002211201000114X

Optimal wave packets in a boundary layer and initial phases of a turbulent spot

S. CHERUBINI[1,2]†, J. -C. ROBINET[2], A. BOTTARO[3] AND P. DE PALMA[1]

[1]DIMEG, Politecnico di Bari, Via Re David 200, 70125 Bari, Italy

[2]SINUMEF Laboratory Arts et Metiers ParisTech, 151, Bd. de l'Hopital, 75013 Paris, France

[3]DICAT, Università di Genova, Via Montallegro 1, 16145 Genova, Italy

(Received 13 June 2009; revised 8 February 2010; accepted 26 February 2010; first published online 27 May 2010)

The three-dimensional global optimal dynamics of a flat-plate boundary layer is studied by means of an adjoint-based optimization in a spatial domain of long – but finite – streamwise dimension. The localized optimal initial perturbation is characterized by a pair of streamwise-modulated counter-rotating vortices, tilted upstream, yielding at the optimal time elongated streaks of alternating sign in the streamwise direction. This indicates that perturbations with non-zero streamwise wavenumber have a role in the transient dynamics of a boundary layer. A scaling law is provided, describing the variation of the streamwise modulation of the optimal initial perturbation with respect to the streamwise domain length and to the Reynolds number. For spanwise-extended domains, a near-optimal three-dimensional perturbation is extracted during the optimization process; it is localized also in the spanwise direction, resulting in a wave packet of elongated disturbances modulated in the spanwise and streamwise directions. The nonlinear evolution of the optimal and near-optimal perturbations is investigated by means of direct numerical simulations. Both perturbations are found to induce transition at lower levels of the initial energy than local optimal and suboptimal perturbations. Moreover, it is observed that transition occurs in a well-defined region of the convected wave packet, close to its centre, via a mechanism including at the same time oscillations of the streaks of both quasi-sinuous and quasi-varicose nature. Hairpin vortices are observed before transition; they have an active role in the breakdown of the streaks and result in a turbulent spot which spreads out in the boundary layer.

1. Introduction

Hydrodynamic stability of wall-bounded shear flows has seen a spectacular progress since the early years of the twentieth century (Orr 1907; Sommerfeld 1908). Theoretical achievements have gone hand-in-hand with experimental and numerical developments aimed at unravelling some of the mysteries of transition to turbulence. The small perturbation analysis of fluid flows has acquired and improved upon, via the development of global-mode concepts, tools of plasma physics (Briggs 1964; Bers 1983), and it is now understood that the impulse response of a channel or boundary-layer flow is a wave packet which may decay, grow algebraically, or exponentially

† Email address for correspondence: s.cherubini@gmail.com

(depending on the Reynolds number) while travelling downstream at the group velocity. The response to an impulse forcing contains all frequencies (in time) and wavenumbers (in space), and this justifies much of the interest behind experimental works onto the evolution of wave packets in boundary layers (Gaster & Grant 1975; Breuer & Landahl 1990; Cohen, Breuer & Haritonidis 1991; Breuer, Cohen & Haritonidis 1997). If the regime is subcritical (i.e. all eigenmodes are damped), only those disturbances with wavenumbers/frequencies for which non-normal growth is allowed might display some amplification. Non-normal growth arises from the constructive interference of damped eigenmodes which are nearly antiparallel, and typically results in the creation of streamwise elongated flow structures, called streaks (Schmid & Henningson 2001). Work along similar lines has been conducted since the eighties, when the concept of 'optimal perturbation' was introduced, generating much hope to fill the gap in the understanding of bypass transition. In most cases, optimal perturbations – within a linearized framework – have been found to consist of pairs of counter-rotating streamwise vortices, capable to elicit streamwise streaks by the lift-up effect (Landahl 1980, 1990). If growth is sufficient, such elongated structures could experience secondary instability and breakdown, due to the inflection of the velocity profiles in their interaction zones (see Schoppa & Hussain 2002; Brandt, Schlatter & Henningson 2004). At large enough values of the Reynolds number, nonlinear effects might kick in, and an impulse perturbation of sufficiently large amplitude typically induces bypass transition by generating a turbulent 'spot', which rapidly grows and spreads, leading the flow – in a frame of reference moving at the spot velocity – towards the fully turbulent state.

Since the early observations by Emmons (1951), many studies have been dedicated to the interior structure of turbulent spots, their shapes, spreading rates and the mechanism of their rapid growth (Wygnanski, Sokolov & Friedman 1976; Gad-el Hak, Blackwelder & Riley 1981; Perry, Lim & Teh 1981; Chambers & Thomas 1983; Barrow *et al.* 1984; Henningson, Spalart & Kim 1987; Sankaran, Sokolov & Antonia 1988; Lundbladh & Johansson 1991; Bakchinov, Grek & Kozlov 1992; Henningson, Lundbladh & Johansson 1993; Singer 1996; Matsubara & Alfredsson 2001). Recently, a new scenario of transition has emerged, based on vortex generation in wall bounded flows (Marusic 2009). The relevance of hairpin-shaped structures in the sustainment of wall turbulence has been proved in the past decades by several experimental (Head & Bandyopadhyay 1981) and numerical (Adrian 2007) studies. A clear evidence of the preponderance of hairpin vortices in the late stages of transition of a boundary-layer flow has been provided conclusively by Wu & Moin (2009). By means of a direct numerical simulation, they have observed the onset of hairpin structures emerging from Λ-shaped vortices excited by free-stream turbulence.

Nothing has however been done so far to identify the initial, localized states which most easily bring the flow on the verge of turbulent transition via the formation of a spot. In other words, since in most practical cases boundary layers undergo transition by receptively selecting and amplifying exogenous disturbances, such as those arising from the presence of localized roughness elements or gaps on the wall, it makes sense to inquire on the initial spatially localized flow patterns which most easily amplify and cause breakdown. In fact, the transition mechanism based on the – by now classical – local optimal perturbation concept is very seductive, since it brings into play some of the main ingredients present in transitional flow fields – streaks and vortices, with the notable exception of the travelling waves (see Faisst &

Eckhardt 2003; Wedin & Kerswell 2004) – but has the limitation of focusing onto a single wavenumber/frequency at a time, plus that of neglecting nonlinear effects. When a direct simulation is performed to assess the effectiveness of linear optimal perturbations in triggering transition, the outcome is rather disappointing (Biau & Bottaro 2009), and suboptimal disturbances are found to be much more efficient than optimals.

In this work an attempt is made to identify initial localized disturbances capable to provoke breakdown to turbulence effectively in a boundary-layer flow over a flat plate. We aim to optimize not simply an initial state (at $x = 0$ or $t = 0$) characterized by a single wavenumber and/or frequency, but a wave packet, localized in the streamwise direction (and eventually also of limited spanwise extent), composed by the superposition of small-amplitude monochromatic waves. The procedure to find such a packet is that of the classical optimization theory, with the remarkable difference that the optimization is carried out for a non-parallel boundary-layer flow in a localized domain, and that no assumption is made on the shape and the frequency spectrum of the perturbation in all directions. To assess whether the optimal localized flow state is effective in provoking breakdown, direct numerical simulations are then performed, highlighting the importance of nonlinear effects which lie at the heart of the initiation of a turbulent spot.

The paper is organized as follows. In § 2, after the definition of the problem, the numerical tools are briefly described, namely the three-dimensional direct-adjoint optimization method and the global eigenvalue model. In § 3, a thorough discussion of the results of the linear optimization analysis is provided, focusing on the streamwise and the spanwise dynamics. Furthermore, the 'near-optimal' perturbation is presented and discussed. Then, the results of nonlinear simulations are provided, and the features of the transition mechanism are described. Finally, some conclusions are drawn.

2. Problem formulation

2.1. *Governing equations*

The behaviour of a three-dimensional incompressible flow is governed by the Navier–Stokes equations:

$$\left.\begin{aligned} \boldsymbol{u}_t + (\boldsymbol{u}\cdot\nabla)\boldsymbol{u} &= -\nabla\pi + \frac{1}{Re}\nabla^2\boldsymbol{u}, \\ \nabla\cdot\boldsymbol{u} &= 0, \end{aligned}\right\} \tag{2.1}$$

where $\boldsymbol{u}$ is the velocity vector and π is the pressure. Dimensionless variables are defined with respect to the inflow boundary-layer displacement thickness δ^* and to the free-stream velocity U_∞ so that the Reynolds number is $Re = U_\infty\delta^*/\nu$, where ν is the kinematic viscosity. Most of the computations have been carried out at $Re = 610$. Several computational domains are employed, the reference one having dimensions $L_x = 400$, $L_y = 20$ and $L_z = 2Z = 10.5$, x, y and z being the streamwise, wall-normal and spanwise directions, respectively. The inlet boundary is placed at $x_{in} = 200$ downstream of the leading edge of the wall, whereas the outlet one is placed at $x_{out} = 600$, for the reference domain. For the base flow computations and the direct numerical simulation (DNS), the following boundary conditions are used. At inlet points, a Blasius boundary-layer profile is imposed for the streamwise and wall-normal components of the velocity vector, and the spanwise component is set to

zero. At outlet points, a standard convective condition is employed. At the bottom wall, the no-slip boundary condition is prescribed. At the upper-boundary points, the Blasius solution is imposed for the wall-normal component of the velocity, and the spanwise velocity component and the vorticity are set to zero. Finally, in the spanwise direction, periodicity is imposed for the three velocity components. Details of the numerical method are provided in the Appendix.

2.2. *Three-dimensional direct-adjoint optimization*

The linear behaviour of a perturbation $\boldsymbol{q}=(u, v, w, p)^T$ evolving in a laminar incompressible flow over a flat plate is studied by employing the Navier–Stokes equations linearized around the two-dimensional steady state $\boldsymbol{Q}=(U, V, 0, P)^T$. A zero-perturbation condition is chosen for the three velocity components at the x and y boundaries, whereas periodicity of the perturbation is imposed in the spanwise direction. The disturbance is allowed to smoothly exit from the domain by using a fringe region, whose characteristics are described in the Appendix, implemented by adding to the equations a forcing term in a limited region for $x > x_{out}$.

In order to identify the perturbation at $t=0$, which is able to produce the largest disturbance growth at any given target time T, a Lagrange multiplier technique is used (Zuccher, Luchini & Bottaro 2004). Let us define the disturbance energy density as

$$E(t)=\int_{-Z}^{Z}\int_{o}^{L_y}\int_{x_{in}}^{x_{out}}(u^2(t)+v^2(t)+w^2(t))\,\mathrm{d}x\,\mathrm{d}y\,\mathrm{d}z; \tag{2.2}$$

the objective function of the procedure is the energy of the perturbations at the target time $t=T$, i.e. $E(T)$. The Lagrange multiplier technique consists in seeking extrema of the augmented functional $\mathscr{L}$ written as

$$\begin{aligned}\mathscr{L} = E(T) &+ \int_{-Z}^{Z}\int_{o}^{L_y}\int_{x_{in}}^{x_{out}}\int_{0}^{T} a(u_x+v_y+w_z)\,\mathrm{d}t\,\mathrm{d}x\,\mathrm{d}y\,\mathrm{d}z \\ &+ \int_{-Z}^{Z}\int_{o}^{L_y}\int_{x_{in}}^{x_{out}}\int_{0}^{T} b\left(u_t+(uU)_x+U_y v+Vu_y+p_x-\frac{u_{xx}+u_{yy}+u_{zz}}{Re}\right)\mathrm{d}t\,\mathrm{d}x\,\mathrm{d}y\,\mathrm{d}z \\ &+ \int_{-Z}^{Z}\int_{o}^{L_y}\int_{x_{in}}^{x_{out}}\int_{0}^{T} c\left(v_t+Uv_x+(vV)_y+uV_x+p_y-\frac{v_{xx}+v_{yy}+v_{zz}}{Re}\right)\mathrm{d}t\,\mathrm{d}x\,\mathrm{d}y\,\mathrm{d}z \\ &+ \int_{-Z}^{Z}\int_{o}^{L_y}\int_{x_{in}}^{x_{out}}\int_{0}^{T} d\left(w_t+Uw_x+Vw_y+p_z-\frac{w_{xx}+w_{yy}+w_{zz}}{Re}\right)\mathrm{d}t\,\mathrm{d}x\,\mathrm{d}y\,\mathrm{d}z \\ &+ \lambda_0\left[E(0)-E_0\right].\end{aligned} \tag{2.3}$$

The linearized Navier–Stokes equations (direct problem) and the value of the energy at $t=0\,(E_0)$ have been imposed as constraints and a, b, c, d, λ_0 are the Lagrange multipliers. Integrating by parts and setting to zero the first variation of $\mathscr{L}$ with

respect to u, v, w, p leads to the adjoint equations:

$$\left.\begin{aligned} b_t + b_x U + (bV)_y - cV_x + a_x + \frac{b_{xx}}{Re} + \frac{b_{yy}}{Re} + \frac{b_{zz}}{Re} = 0, \\ c_t + (cU)_x + c_y V - bU_y + a_y + \frac{c_{xx}}{Re} + \frac{c_{yy}}{Re} + \frac{c_{zz}}{Re} = 0, \\ d_t + (dU)_x + (dV)_y + a_z + \frac{d_{xx}}{Re} + \frac{d_{yy}}{Re} + \frac{d_{zz}}{Re} = 0, \\ b_x + c_y + d_z = 0, \end{aligned}\right\} \tag{2.4}$$

where $\boldsymbol{q}^\dagger = (a, b, c, d)^T$ is now identified as the adjoint vector. By using the boundary conditions of the direct problem, one obtains

$$\left.\begin{aligned} b = 0\,, \quad c = 0\,, \quad d = 0\,, \quad \text{for } y = 0 \text{ and } y = L_y, \\ b = 0\,, \quad c = 0\,, \quad d = 0\,, \quad \text{for } x = x_{in} \text{ and } x = x_{out}, \end{aligned}\right\} \tag{2.5}$$

plus optimality and compatibility conditions (Zuccher *et al.* 2004):

$$-b + 2\lambda_0 u = 0\,, \quad -c + 2\lambda_0 v = 0\,, \quad -d + 2\lambda_0 w = 0 \quad \text{for } t = 0, \tag{2.6}$$

$$b + 2u = 0\,, \quad c + 2v = 0\,, \quad d + 2w = 0 \quad \text{for } t = T. \tag{2.7}$$

The direct and adjoint equations are parabolic in the forward and backward time direction, respectively, so that they can be solved by a coupled iterative approach. The optimization procedure for a chosen target time T can be summarized as follows:

(*a*) An initial guess is taken for the initial condition $\boldsymbol{q}_0$, at $t = 0$, with an associated initial energy E_0.

(*b*) The direct problem is integrated from $t = 0$ to $t = T$.

(*c*) At $t = T$, the initial state for the adjoint problem is provided by the compatibility condition (2.7).

(*d*) The adjoint problem (2.4) is integrated backward in time from $t = T$ to $t = 0$, starting from the initial state of step (*c*).

(*e*) At $t = 0$, the optimality condition (2.6) determines the new initial state $\boldsymbol{q}_0$ for the direct problem and the Lagrange multiplier λ_0 is chosen in order to satisfy the constraint $E(0) = E_0$.

(*f*) The objective function $E(T)$ is evaluated in order to assess if its variation between two successive iterations is smaller than a chosen threshold. In such a case the loop is stopped, otherwise the procedure is restarted from step (*b*).

The Appendix provides the details of the numerical method employed for the integration of the direct and adjoint equations, the performance of the optimization procedure, as well as the convergence study.

2.3. *Global eigenvalue analysis*

The optimization is also carried out by the global model described in Alizard & Robinet (2007), the perturbation being characterized by only one spanwise wavenumber β, so that $\boldsymbol{q}(x, y, z, t) = \tilde{\boldsymbol{q}}(x, y, t)\exp(\mathrm{i}\beta z)$. The shape function is decomposed in temporal modes as

$$\tilde{\boldsymbol{q}}(x, y, t) = \sum_{k=1}^{N} \kappa_k^0 \, \hat{\boldsymbol{q}}_k(x, y) \exp(-\mathrm{i}\omega_k t)\,, \tag{2.8}$$

where N is the total number of modes, $\hat{\boldsymbol{q}}_k$ are the eigenvectors, ω_k are the (complex) eigenvalues and κ_k^0 represents the initial energy of each mode. Substitution of such

a decomposition into the linearized Navier–Stokes equations leads to the eigenvalue problem of the form

$$(\boldsymbol{A} - \mathrm{i}\omega_k \boldsymbol{B})\,\hat{\boldsymbol{q}}_k = \boldsymbol{0}, \quad k = 1, \ldots, N. \tag{2.9}$$

The details of the definition of the matrices $\boldsymbol{A}$ and $\boldsymbol{B}$ can be found in Alizard & Robinet (2007). At the free-stream and inlet boundaries, a zero-perturbation condition is imposed, whereas, at the outlet points, a homogeneous Neumann condition is prescribed. In order to optimize the disturbance energy density, for a given initial value of the same, the maximum energy gain obtainable at the generic time t over all possible initial conditions $\boldsymbol{u}_0$ is defined as

$$G(t) = \max_{\boldsymbol{u}_0 \neq 0} \frac{E(t)}{E(0)}. \tag{2.10}$$

By decomposing the perturbation into the basis of the eigenmodes, it is possible to rewrite (2.10) in the following form:

$$G(t) = \|\boldsymbol{F} \exp(-\mathrm{i}t\boldsymbol{\Lambda})\boldsymbol{F}^{-1}\|_2^2, \tag{2.11}$$

where $\boldsymbol{\Lambda}$ is the diagonal matrix of the eigenvalues ω_k, and $\boldsymbol{F}$ is the Cholesky factor of the energy matrix $\boldsymbol{M}$ of components

$$M_{ij} = \int_o^{L_y} \int_{x_{in}}^{x_{out}} (\hat{u}_i^* \hat{u}_j + \hat{v}_i^* \hat{v}_j + \hat{w}_i^* \hat{w}_j)\,\mathrm{d}x\,\mathrm{d}y, \quad i, j = 1, \ldots, N, \tag{2.12}$$

where the superscript '*' denotes complex-conjugate. Finally, the maximum amplification at time t and the corresponding optimal initial condition $\boldsymbol{u}_0$ are computed by a singular value decomposition of the matrix $\boldsymbol{F} \exp(-\mathrm{i}t\boldsymbol{\Lambda})\boldsymbol{F}^{-1}$ (Schmid & Henningson 2001). The Appendix provides the details of the numerical method employed for the global eigenvalue analysis, and the convergence study.

3. Results

3.1. *The linear optimal dynamics*

Direct-adjoint computations are performed at $Re = 610$, for a domain with dimensions $L_x = 400$, $L_y = 20$, $L_z = 10.5$, the value of L_z being selected in order to obtain the largest amplification, as shown in § 3.1.2. The optimal energy gain $G(t)$ is found to reach, at the chosen convergence level $e = 10^{-5}$ (see the Appendix), a maximum of about $G_{max} \approx 736$, at time $T_{max} \approx 247$. Such a value is greater than that found by a local parallel flow optimization (Corbett & Bottaro 2000) at the same Reynolds number.

In order to get some insight into the amplification mechanism, the evolution of the optimal perturbation in time is analysed. In figure 1 the initial (at $t = 0$) optimal perturbation is depicted on the plane z–y at the streamwise position $x = 450$. The optimal spatially localized initial disturbance is characterized by a counter-rotating vortex pair in the z–y plane. In previous works, several authors (see Farrell 1988; Butler & Farrell 1992; Corbett & Bottaro 2000; Luchini 2000; Schmid 2000) have optimized locally the time amplification in terms of the energy density of a perturbation characterized by a given wavenumber in both the streamwise and spanwise directions (denoted respectively by α and β). Those authors have found that the local optimal perturbation is characterized by a counter-rotating vortex pair in the z–y plane, without any modulation in the streamwise direction ($\alpha = 0$), amplified in time by means of the 'lift-up' mechanism (Landahl 1980). In the present case, where the perturbation has no pre-assigned wavelength, a modulation is found in

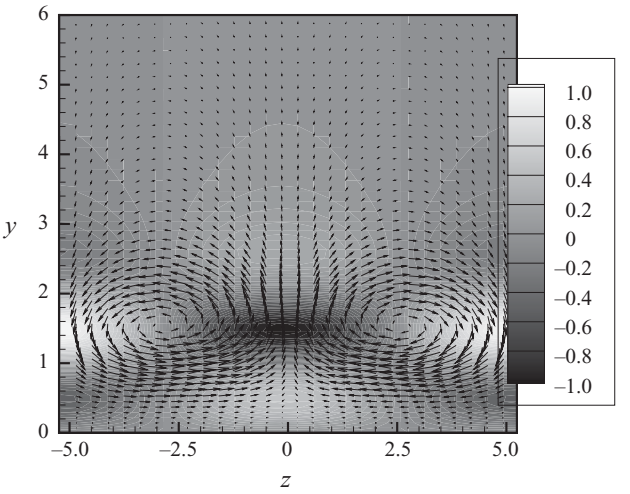

FIGURE 1. Optimal initial perturbation on the $x = 450$ plane computed for the target time $t = T_{max}$ and $Re = 610$. The vectors represent the v and w components, whereas the shading is relative to the normalized streamwise velocity.

the x direction, the perturbation being composed by upstream-elongated structures with velocity components of alternating signs also in the x–y plane, as shown by the iso-surfaces of the streamwise, wall-normal and spanwise velocity in figure 2. The time evolution of such an optimal solution shows that the perturbation tilts downstream via the Orr mechanism (Schmid & Henningson 2001), while being amplified by the lift-up mechanism, resulting at the optimal time T_{max} in streaky structures with alternating-sign velocity components in the x direction, as displayed in figure 3. Indeed, the amplification of the initial perturbation is also due to the Orr mechanism and to the spatial growth related to the non-parallelism of the flow. In order to estimate the importance of such effects, a direct-adjoint optimization is performed using a two-dimensional domain with $L_x = 400$ and $L_y = 20$, for which the lift-up mechanism is inhibited. In this case the energy gain reaches only a maximum value of 80 at time $t \approx 650$, which is very low with respect to the maximum amplification of the three-dimensional case, proving that both the Orr mechanism and the convective spatial growth have a secondary role in the three-dimensional optimal dynamics at $Re = 610$. In order to find how large is the contribution of the convective spatial growth mechanism, the two-dimensional optimization is also performed using the parallel flow obtained by reproducing at each abscissa the inlet base flow profile. The optimization gives an optimal value of the energy gain equal to 35, indicating that about one half of the two-dimensional energy growth is due to the convective amplification induced by the non-parallelism of the base flow.

3.1.1. *Analysis of the streamwise modulation of the optimal perturbation*

To investigate the influence of the longitudinal domain length on the transient amplification, two computations are performed with $L_{x2} = 800$ and $L_{x3} = 1200$, equal to two and three times the length of the reference domain. These two domains are discretized by 1001 and 1501 points in the streamwise direction, respectively. As shown in figure 4, the optimal energy gain reaches a peak of 1250 at $T \approx 490$ using L_{x2}, and of 1720 at $T \approx 821$ using L_{x3}, increasing of about 500 and 1000 units with respect to the value of G_{max} obtained in the reference case. Such a strong increase of

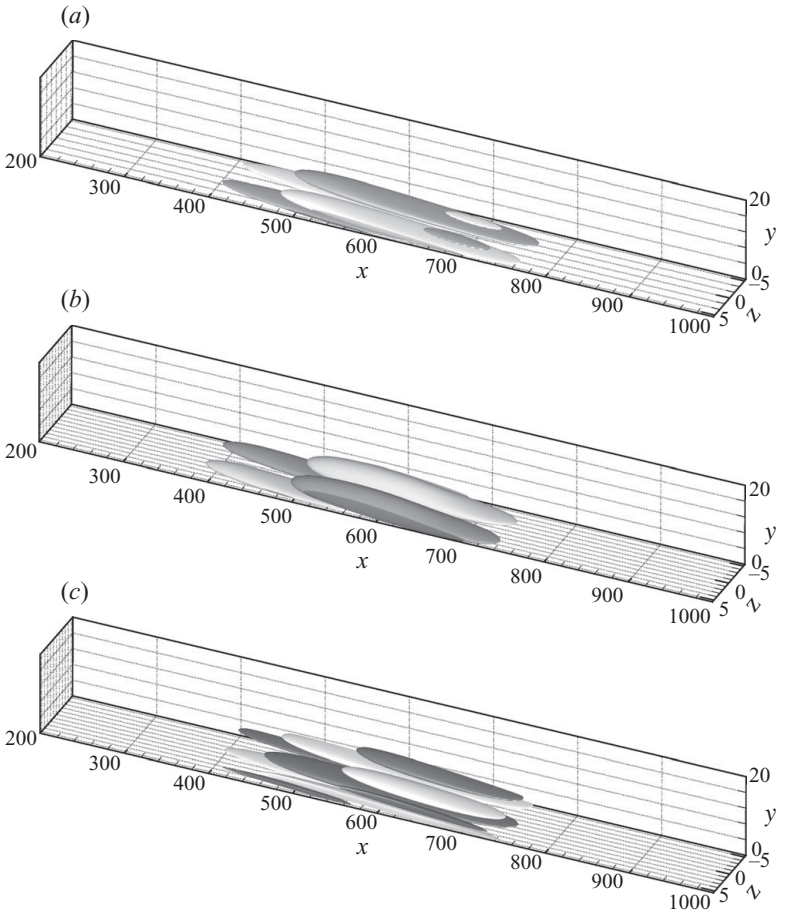

FIGURE 2. Iso-surfaces of the streamwise (a), wall-normal (b) and spanwise (c) velocity components of the optimal initial perturbation at $Re = 610$, for a longitudinal domain length $L_x = 800$. Light and dark surfaces indicate positive and negative values of the velocity components, respectively. The absolute values of their magnitude are 0.01 for the streamwise, 0.1 for the wall-normal, and 0.22 for the spanwise component. All the perturbations are normalized by the maximum value of the spanwise velocity component.

the energy gain with the longitudinal length of the domain can be mostly ascribed to a combined effect of the Orr mechanism and of the spatial amplification due to the non-parallel flow. Indeed, a two-dimensional direct-adjoint optimization performed using $L_{x2} = 800$ predicts again an increase of about 500 units for the $G(t)$ peak with respect to the value found using the reference domain with $L_{x1} = 400$. Moreover, the value of the optimal time increases linearly with the streamwise domain length. This could be expected by considering that the perturbation is convected by the base flow through the whole domain while amplifying itself, so that $t \propto L_x/U_\infty$. The effects of the variation of the domain length on the shape of the optimal perturbation are shown in figure 5, where the optimal initial solutions are provided for L_{x1} and L_{x2} using dashed and solid lines, respectively. In order to allow a meaningful comparison, the perturbation is plotted using normalized coordinates: the wall-normal self-similar coordinate $\eta = y\sqrt{Re/x}$, and the scaled abscissa $\bar{x} = xL_{x_1}/L_x$. It can be noticed that the longitudinal extent, the inclination and the modulation of the perturbations are

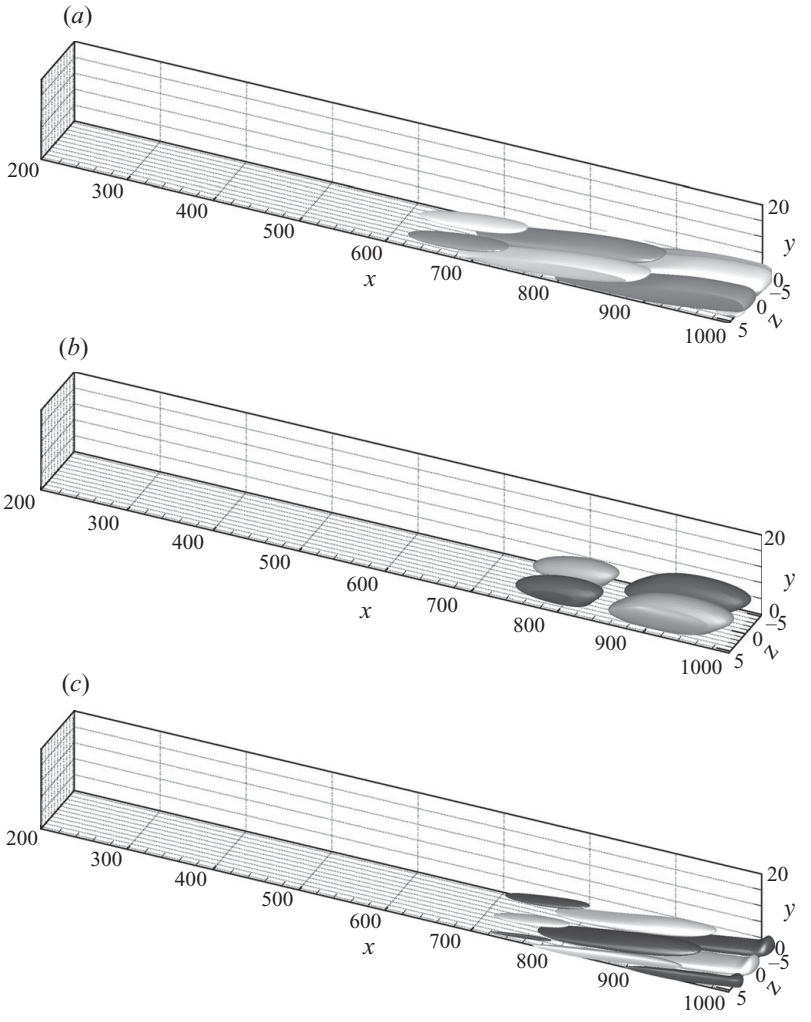

FIGURE 3. Iso-surfaces of the streamwise (a), wall-normal (b) and spanwise (c) velocity components of the optimal disturbance at $t = T_{max}$. Light and dark surfaces indicate positive and negative values of the velocity components, respectively. The absolute values of their magnitude are 1.8 for the streamwise, 0.1 for the wall-normal, and 0.5 for the spanwise component. All the perturbations are normalized by the maximum value of the spanwise velocity component at $t = 0$.

approximately the same, meaning that, when observed in normalized coordinates, the result of the optimization depends mildly on the streamwise domain size considered to compute the objective function. To verify such a result, the characteristic streamwise wavenumber (α_c), defined as the most amplified wavenumber recovered in the initial optimal perturbation by means of a spatial Fourier transform, is extracted from the optimal perturbation computed at different target times for the three domain lengths L_{x1}, L_{x2}, L_{x3} and scaled by L_x/L_{x_1}. The three normalized curves of α_c are plotted in figure 6 with respect to the scaled time $\bar{T} = T L_{x_1}/L_x$. The three curves collapse reasonably well onto one another, confirming the result that, using normalized coordinates, the shape of the optimal perturbation is approximately invariant with respect to the longitudinal length used in the optimization. Such a result allows us to

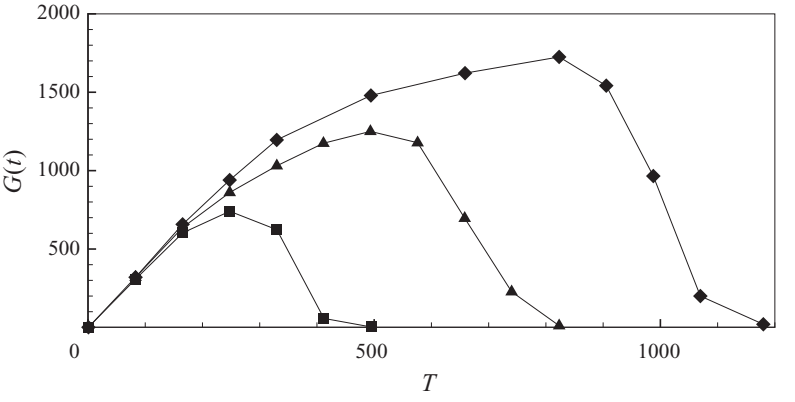

FIGURE 4. Envelope of the optimal energy gain computed by the direct-adjoint method at $Re = 610$ for three longitudinal domain lengths, $L_{x1} = 400$ (■), $L_{x2} = 800$ (▲), $L_{x3} = 1200$ (◆).

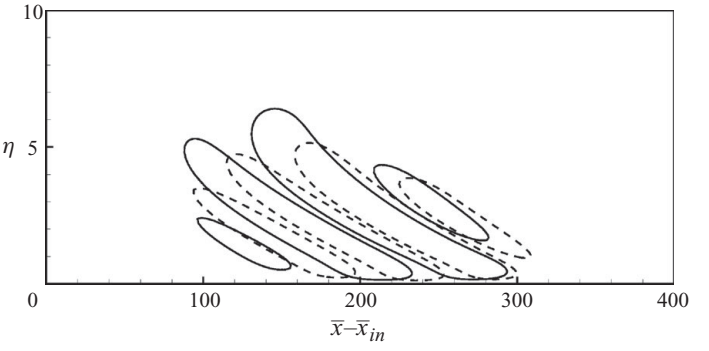

FIGURE 5. Contours of the streamwise velocity component of the optimal initial perturbation for L_{x1} (dashed contours) and L_{x2} (solid contours) at $Re = 610$. The perturbations have been normalized by their maximum value; contours with absolute value equal to 0.15 are shown.

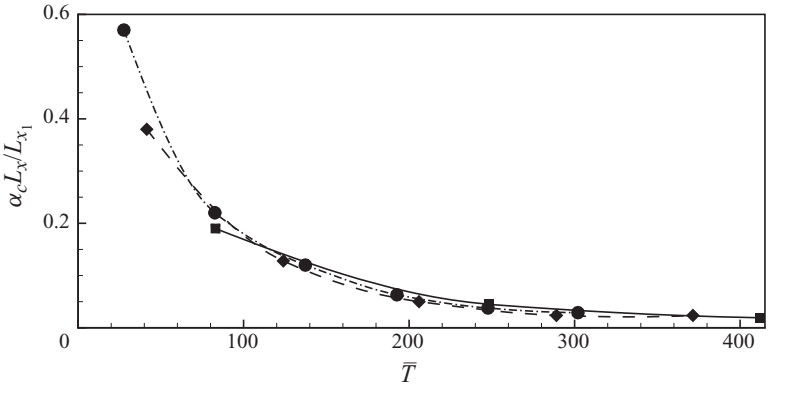

FIGURE 6. Normalized most amplified longitudinal wavenumber versus the normalized target time at $Re = 610$, for $L_{x1} = 400$ (■), $L_{x2} = 800$ (◆) and $L_{x3} = 1200$ (●).

reduce the number of independent parameters in the optimization, as the streamwise wavelength of the perturbation scales with L_x. It is noteworthy that the characteristic streamwise wavenumber, α_c, is rather high at small times and decreases with time towards an asymptotic value.

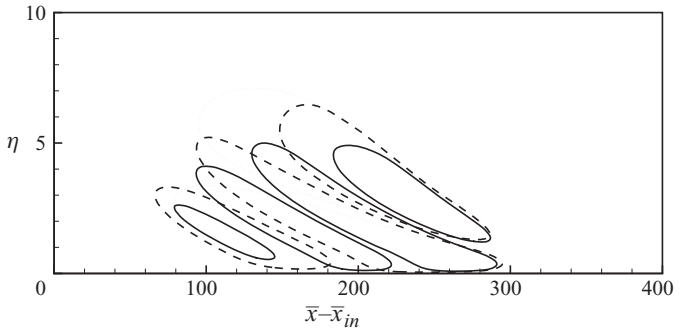

FIGURE 7. Contours of the spanwise velocity component of the optimal initial perturbation for $Re = 610$ (solid contours), $Re = 300$ (dashed contours) and $Re = 150$ (dotted contours). The perturbations have been normalized by their maximum value; the contours with absolute value equal to 0.15 are shown.

A similar analysis is carried out focusing on the influence of the Reynolds number on the optimal initial perturbation: the direct-adjoint optimization is performed for two smaller Reynolds numbers, $Re = 300$ and $Re = 150$. Both values of Re are chosen with the aim of keeping the entire flow, from the inlet to the outlet, locally stable with respect to Tollmien–Schlichting modes, in order to ensure that the x-modulation of the optimal perturbation is not due to the interaction of local optimals with such modes. Figure 7 provides the spanwise velocity component contours of the optimal initial perturbation computed at $Re = 610$ (solid line), $Re = 300$ (dashed line), $Re = 150$ (dotted line) and $L_x = L_{x1}$. At all values of Re, the optimal perturbation displays a modulation in the x-direction. Moreover, the streamwise extent of the perturbation in normalized coordinates is found to vary, with an increase of the characteristic wavenumber with Re. To assess the variation of the streamwise modulation with the Reynolds number, the characteristic streamwise wavenumber, α_c, is extracted from the optimal initial perturbations computed for different target times and for the three values of Re. The values of α_c, shown in figure 8(a) for each value of the target time ($T = 166, 247, 330, 420$, represented by squares, diamonds, circles and triangles, respectively) are found to scale well with the square root of the Reynolds number. Indeed, dividing the α_c values by the square root of the Reynolds number, the three curves collapse onto each other for sufficiently large times (see figure 8b). Therefore, the results indicate that α_c behaves as

$$\alpha_c \propto \frac{\sqrt{Re}}{L_x}, \tag{3.1}$$

providing the variation of the optimal streamwise modulation with the domain length employed to integrate the objective function and with the Reynolds number. Using such a scaling law, one may recover the classical result on the optimal temporal growth in a parallel boundary-layer flow, since it yields $\alpha_c \to 0$ for an infinitely long domain.

Once the dependence of the characteristic streamwise modulation on the independent parameters of the optimization, Re and L_x, is analysed, the origin of such a modulation needs to be investigated. Since the global optimal perturbation is found to be characterized by more than one wavenumber in x, it is conjectured that it can originate from a superposition of local optimal single-wavenumber perturbations. Thus, following the method of Corbett & Bottaro (2000), a local optimization is

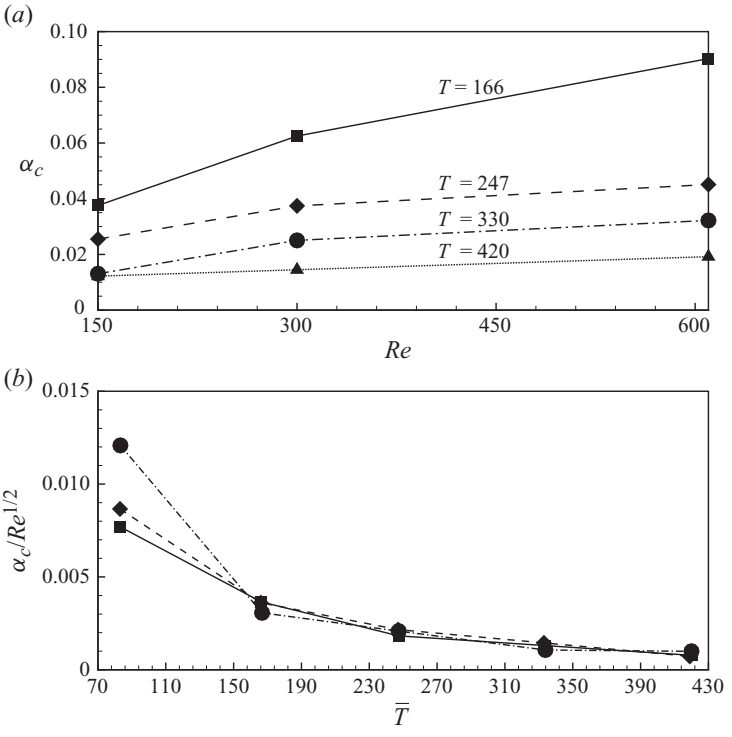

FIGURE 8. (*a*) Most amplified longitudinal wavenumber versus the Reynolds number for $T = 166$ (—), $T = 250$ (– – –), $T = 330$ (– · – · –) and $T = 420$ (· · · ·); (*b*) normalized most amplified longitudinal wavenumber versus the normalized target time for $Re = 610$ (■), $Re = 300$ (◆) and $Re = 150$ (●).

performed using the inlet velocity profile as a base flow. Such an optimization is carried out for 160 values of α varying in the range from -0.4 to 0.4. To allow a meaningful comparison, the wavenumber of largest module, 0.4, is chosen larger than the largest streamwise wavenumber obtained by a spatial Fourier transform of the global optimal perturbation. Similar criterion is used to pick the wavenumber of smallest absolute value, 0.005. A three-dimensional perturbation is thus reconstructed as a superposition of the local optimal ($\alpha = 0$) and all the suboptimal ($\alpha \neq 0$) solutions computed at the target time T_{max}, namely

$$\boldsymbol{q}(x, y, z) = \sum_{j=1}^{n} \kappa_j \, \bar{\boldsymbol{q}}_j(y) \exp(\mathrm{i}\beta z - \mathrm{i}\alpha_j x), \tag{3.2}$$

where $n = 160$, $\bar{\boldsymbol{q}}_j(y)$ is the result of the local optimization at a given value of α (see Corbett & Bottaro 2000) and κ_j is linked to the energy of each single-wavenumber perturbation. For the present analysis, a value of β equal to 0.6 is employed, corresponding to the optimal spanwise wavenumber (see § 3.1.2). At $t = 0$, all the locally optimized perturbations are superposed with initial energy equal to 1. Figure 9 shows for $t = T_{max}$ that such a reconstruction is able to qualitatively reproduce packets of counter-rotating vortices as well as the x-modulated streak-like structures, demonstrating that the three-dimensional dynamics of a boundary layer is characterized by the superposition of modes with zero and non-zero streamwise wavenumber. The analysis of the variation of α_c with time is also performed for the three-dimensional

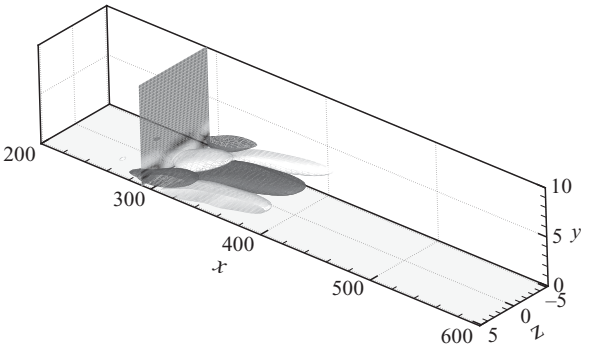

FIGURE 9. Iso-surfaces of the streamwise velocity component of the perturbation obtained at $t = T_{max}$ by the superposition of local optimal and suboptimal perturbations for $Re = 610$. Light and dark surfaces indicate positive and negative values of the velocity components, respectively, with absolute value equal to 0.75. The perturbation is normalized by its maximum value.

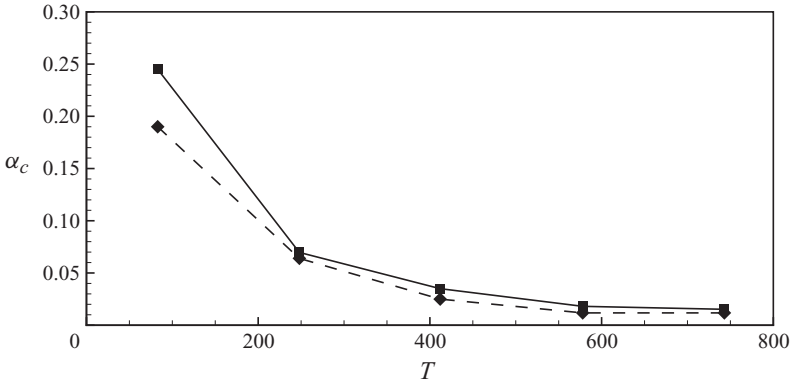

FIGURE 10. Most amplified longitudinal wavenumber versus the target time for $Re = 610$, obtained by the direct-adjoint method with $L_x = 800$ (◆) and by the superposition of local optimal and suboptimal perturbations (■).

perturbation reconstructed as a superposition of local optimals and suboptimals. As shown in figure 10, the α_c curves obtained from the global optimal perturbation and the superposition of local optimal and suboptimal solutions, for $L_x = 800$, are found to be very close for all times but the smallest ($t = 41$), meaning that such a reconstruction is able to reproduce the streamwise wavenumber dominating the optimal dynamics.

3.1.2. *Analysis of the spanwise modulation of the optimal perturbation*

The effect of the spanwise domain length on the optimal dynamics is analysed by performing the energy optimization for several lengths. Figure 11 shows the behaviour of the maximum optimal energy gain versus the spanwise minimum wavenumber, $\beta_L = (2\pi)/L_z$, computed by means of the global model (squares) and by the direct-adjoint procedure (circles). It is worth to point out that, concerning the global model, the wavenumber of the optimal perturbation is prescribed, $\beta = \beta_L$, whereas, in the direct-adjoint computation, β_L represents the minimum allowed value of the optimal perturbation wavenumber. Since the problem under consideration is homogeneous in the spanwise direction, it is anticipated that the result of the optimization would contain only one wavenumber in that direction, namely the one which is able to induce

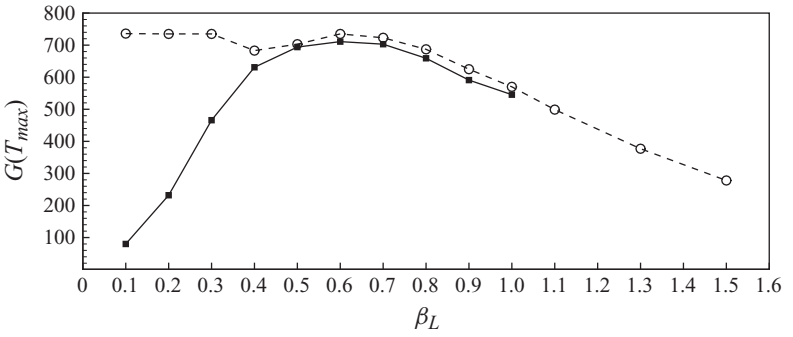

FIGURE 11. Peak value of the optimal energy gain versus the spanwise minimum wavenumber β_L obtained by the global model (■) and by the direct-adjoint method (○) with $\beta_L = (2\pi)/L_z$.

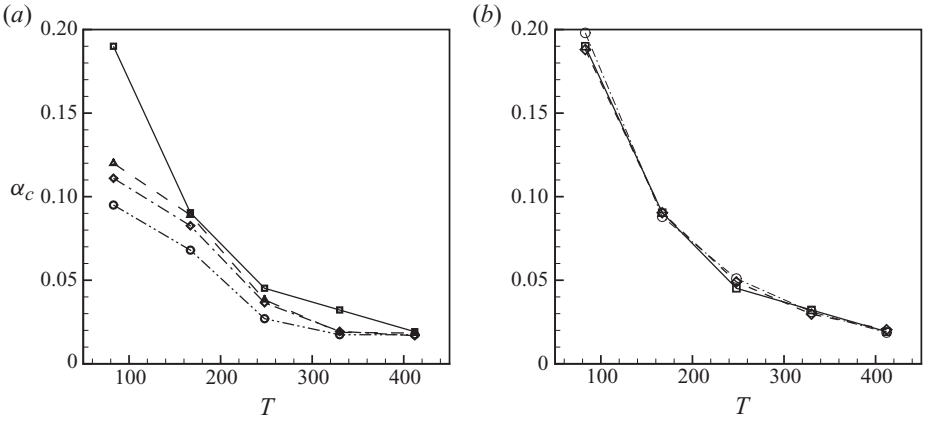

FIGURE 12. Most amplified longitudinal wavenumber versus the target time at $Re = 610$, obtained by the direct-adjoint method for $\beta_L = 0.6$ (□), $\beta_L = 0.8$ (△), $\beta_L = 1.0$ (◇), $\beta_L = 1.3$ (○) (a); and for $\beta_L = 0.6$ (□), $\beta_L = 0.1$ (◇), $\beta_L = 0.035$ (○) (b).

the largest amplification among the multiples of β_L. Thus, for small values of β_L, the two optimization methods would give different results, as one can notice in figure 11. Indeed, the global model predicts a well-defined peak for $\beta_L = 0.6$, hereafter called β_{opt}, corresponding to $L_z = 10.5$, which is very close to the optimal wavenumber computed locally by Corbett & Bottaro (2000). In the direct-adjoint optimization, for high values of β_L, the optimal amplification peaks match those computed by the global model, whereas a plateau is found for subharmonic values of β_{opt}, namely, $\beta_L = 0.1, 0.2, 0.3$. For such values, the wavenumber characterizing the perturbation is equal to β_{opt}, whereas for $\beta_L = 0.4$ one has $\beta = 0.8$. A similar behaviour is found for the optimal time (not shown): for subharmonic values of β_{opt}, the time of maximum growth in the direct-adjoint procedure matches the optimal time found when $\beta = 0.6$, whereas the global model predicts a large increase of the optimal time for low values of β_L.

The effect of the spanwise size of the domain onto the shape of the optimal perturbation is now analysed. Figure 12(a) shows the variation in time of the characteristic wavenumber α_c for several values of $\beta_L > \beta_{opt}$. The values of α_c decrease for increasing β_L, showing a time variation similar to that displayed for $\beta_L = \beta_{opt}$ (solid line). Indeed, they are found to slowly converge to a value different from zero, which is very close to the one achieved asymptotically when $\beta_L = \beta_{opt} = 0.6$. Figure 12($b$)

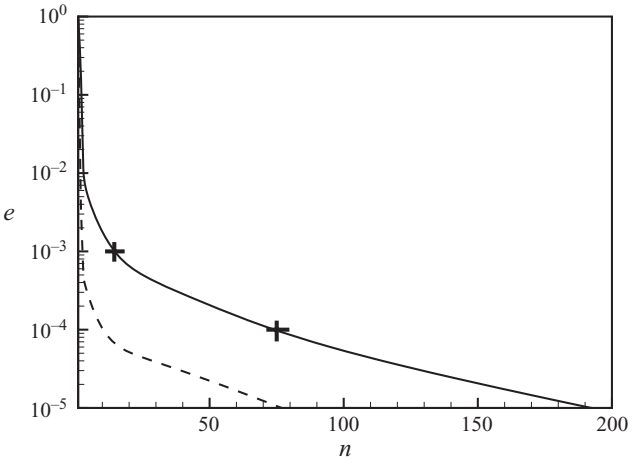

FIGURE 13. Normalized increment of the objective function versus the number of direct-adjoint iterations represented in a semilogarithmic scale for a computation initialized using a wave packet (—) and a single-wavenumber perturbation (– – –) for $T = 247$ and $\beta_L = 0.1$. The crosses indicate the convergence levels at which the 'near-optimal' wave packets have been extracted.

shows the variation of α_c with time for two values of $\beta_L < \beta_{opt}$, more representative of realistic cases. The value $\beta_L = 0.035$ is chosen to be incommensurable with the optimal one. All the curves almost overlap the optimal one, indicating that, for a sufficiently large domain, the streamwise shape of the optimal perturbation matches that obtained for $\beta = \beta_{opt}$. This is true even when the spanwise domain length is not an exact multiple of the optimal one. In conclusion, the three-dimensional optimal perturbation in a boundary layer is characterized, for large spanwise domain lengths (small β_L), by streamwise elongated structures alternated in the x and z directions with an angle $\Theta_{opt} = \arctan(\alpha_{opt}/\beta_{opt})$ ($\Theta_{opt} \approx 4.5^\circ$).

3.2. *The near-optimal linear dynamics*

The results of the previous analysis show that the optimal three-dimensional perturbation is localized in x and characterized by a wide frequency spectrum in the streamwise direction. On the other hand, it is well known that such a perturbation has a spanwise sinusoidal shape since the problem under consideration is homogeneous in the spanwise direction. It could be argued that such a disturbance is not realistic; indeed, in a real framework, disturbances are most likely characterized by a range of frequencies, and not by a monochromatic signal, and are often localized in wave packets, for example when they are caused by a localized roughness element or by a gap on the wall. Thus, a 'near-optimal' perturbation is now focused upon, characterized by the following features:

(*a*) it must show a wide spectrum of spanwise frequencies,
(*b*) it must be localized in both x and z,
(*c*) it must amplify essentially as much as the 'true' global optimal disturbance.

In order to compute such a 'near-optimal' perturbation, an artificial wave packet is built in the two domains of largest spanwise extent (corresponding to $\beta_L = 0.1$ and $\beta_L = 0.035$), by multiplying the optimal single-wavenumber perturbation times an envelope of the form $\exp -(z^2/L_z)$. Such a wave packet is then used as initial guess for the optimization procedure. Figure 13 provides the variation of the objective

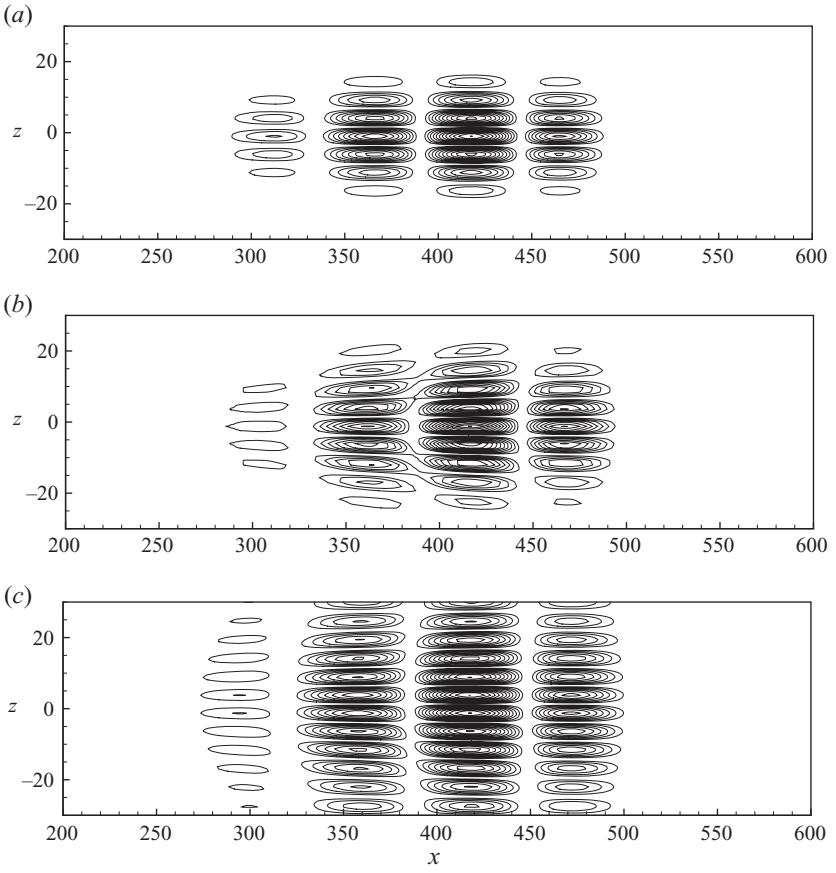

FIGURE 14. Contours of the streamwise component of the perturbation: initial guess (a); intermediate solution at $e_1 = 10^{-3}$ (b); intermediate solution at $e_2 = 10^{-4}$ (c).

function versus the number of iterations for two computations with $\beta_L = 0.1$: the first one, initialized by the artificial wave packet (solid line); the second one, initialized by a single-spanwise-wavenumber perturbation (dashed line). One could observe that both curves experience a marked change in slope and that, in the first case, the convergence is slower. The partially optimized perturbation is extracted at two levels of convergence, e (defined in the Appendix). Figure 14 shows such intermediate solutions at $e_1 = 10^{-3}$ and $e_2 = 10^{-4}$ (indicated with the crosses in figure 13), as well as the wave packet used as the initial guess. It is possible to notice that at e_1 the perturbation is still spanwise localized, although its shape has changed. In particular, the streak-like structures at the edge of the wave packet are inclined with respect to the z-axis, resulting in oblique waves bordering the wave packet. Such a tilting is linked to the superposition of different modes in the spanwise direction. Indeed, Fourier transforms in z of the perturbation at different streamwise locations show that it is composed by many different modes, the spectrum being centred around the optimal wavenumber, as displayed in figure 15(a). On the other hand, at the convergence level e_2 the disturbance is spread out in the whole domain, although a single-spanwise-wavenumber signal is not yet recovered. Most importantly, both solutions, although strongly different in the spanwise direction, are very much amplified, reaching a value of G which differs by less than 1 % from the optimal one ($G(t)_{opt} = 736$, $G(t)_{e_1} = 728$,

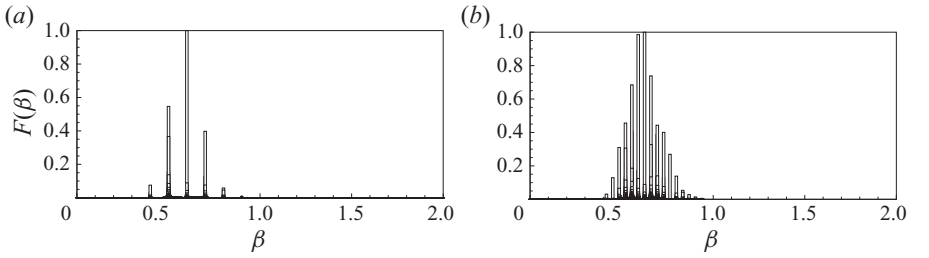

FIGURE 15. Fourier transform in the spanwise direction of the streamwise component of the perturbation at $y=1$, $x=400$, $e_1=10^{-3}$, for $\beta_L=0.1$ (a) and $\beta_L=0.035$ (b). $F(\beta)$ is the normalized Fourier coefficient.

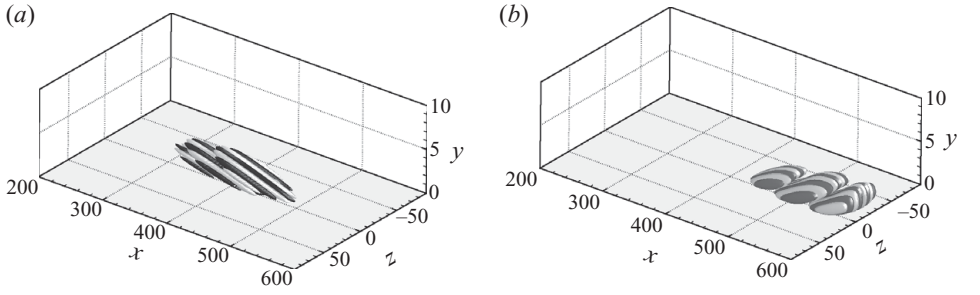

FIGURE 16. Iso-surfaces of the streamwise component of the near-optimal perturbation at the convergence level $e_1=10^{-3}$ for $L_z=180$, at the time instants $t=0$ (a) and $t=T_{max}$ (b). Light and dark surfaces indicate positive and negative values of the velocity components, respectively. Surfaces of absolute value equal to 0.03 and 3 are shown in (a) and (b), respectively. The perturbations are normalized by the maximum value of the spanwise component at $t=0$.

$G(t)_{e_2}=734$). Thus, it is possible to conclude that several near-optimal perturbations exist, intermediate solutions of the optimization process, characterized by different shapes in the spanwise direction, and producing very large growth in the disturbance energy. It is worth to point out that such a result could have been anticipated, since the linearized Navier–Stokes operator is self-adjoint in the spanwise direction for the considered flow. Indeed, no transient energy growth can be produced in the spanwise direction, so that the influence of the spanwise shape of the perturbation on the energy gain is weak with respect to the streamwise and wall-normal ones. Therefore, a perturbation composed by a superposition of wavenumbers in the range $0.5 \leqslant \beta_L \leqslant 0.8$ (like the near-optimal wave packets at e_1 for $\beta_L=0.1$ and $\beta_L=0.035$ whose spectra are shown in figures 15*a* and 15*b*) induces a quasi-optimal energy gain. Finally, it should be pointed out that the self-adjoint character of the Navier–Stokes operator in the spanwise direction may also explain the reduction of the convergence rate observed in figure 13 after level e_1, when the largest residual adjustments of the solution occur in the spanwise direction.

In the following section the nonlinear evolution of a 'near-optimal' wave packet is studied, using the intermediate solution extracted at $e_1=10^{-3}$. Figures 16(a) and 16(b) show such a state at $t=0$ and $t=T_{max}$, respectively, for $\beta_L=0.035$.

3.3. *The nonlinear dynamics*

Although the optimal perturbation computed in the previous section is able to induce a very significant growth of the disturbance energy density in a linearized framework,

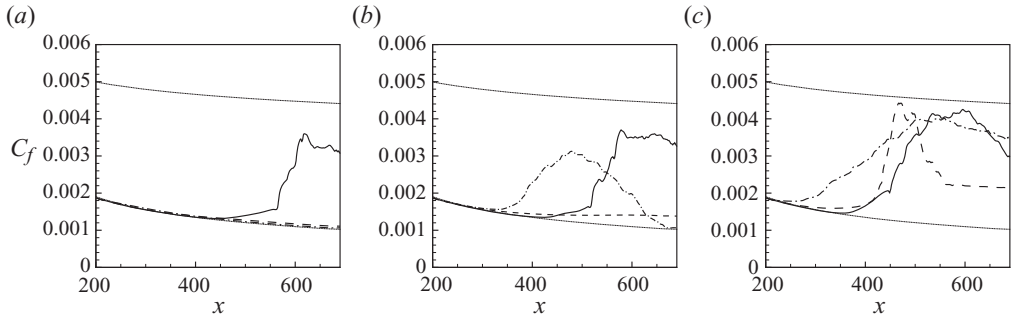

FIGURE 17. Distribution of the mean skin friction coefficient C_f at $t = 700$ for the base flow initially perturbed by: the global three-dimensional optimal (—); the local optimal with $\alpha = 0$ (– – –); the suboptimal with $\alpha = \beta_{opt}$ (– · – · –). Three initial energy levels are considered: $E_0 = 0.5$ (*a*); $E_0 = 2$ (*b*); and $E_0 = 10$ (*c*). The lowest and highest thin lines represent the theoretical distributions of the mean skin friction coefficient for a laminar and a turbulent boundary layer, respectively.

it is not straightforward that it should effectively provoke transition. Therefore, the investigation of the nonlinear evolution of such a global optimal state is worthwhile.

Simulations of the Navier–Stokes equations are thus performed after superposing the initial optimal disturbance (with a given amplitude) to the base flow. The optimal transversal domain length $L_z = 10.5$ and a streamwise length of $L_x = 490$ are chosen. To allow a comparison with some of the most probable transition mechanisms already known in the literature, a direct numerical simulation is performed also for the evolution of the local optimal (with $\alpha = 0$) and suboptimal (with $\alpha = \beta_{opt}$) perturbation superposed to the base flow, using the same initial energy as for the global optimal case. Figure 17 shows the mean skin friction coefficient, C_f, obtained in the simulations initialized with three initial energies: $E_{0(a)} = 0.5$, $E_{0(b)} = 2$ and $E_{0(c)} = 10$. The lowest and highest thin lines in figures 17 represent the theoretical distributions of the laminar and turbulent skin friction coefficient in a boundary layer, whereas the solid, dashed and dash-dotted lines are the mean skin friction coefficients obtained in the simulations initialized using the global optimal, the local optimal and the local suboptimal perturbation, respectively. The value of the energy $E_{0(a)}$ is found to be the lowest one able to cause transition in the flow perturbed by the global optimal disturbance. Indeed, figure 17(*a*) shows that in such a case the mean skin friction (solid line), which initially follows the theoretical laminar value, rises up towards the turbulent value. On the other hand, the skin friction coefficient curves relative to the local optimal and suboptimal cases lay on the theoretical laminar curve for $E_{0(a)} = 0.5$. Figure 17(*b*, *c*) shows that the suboptimal x-modulated perturbation begins to induce transition for the energy value $E_{0(b)}$, whereas the zero-streamwise wavenumber perturbed flow experiences transition only for a rather large initial disturbance energy, $E_{0(c)}$. It is worth observing that such an initial energy value results in a streak amplitude prior to transition of 28 % of the free-stream velocity value, which is close to the threshold amplitude identified by Andersson *et al.* (2001) for the sinuous breakdown of streaks. Moreover, such results confirm those by Biau, Soueid & Bottaro (2008), and point out the effectiveness of suboptimal perturbations in inducing transition. It is interesting to observe that, when initialized by the global optimal disturbance, transition always starts around $x = 400$, almost irrespective of

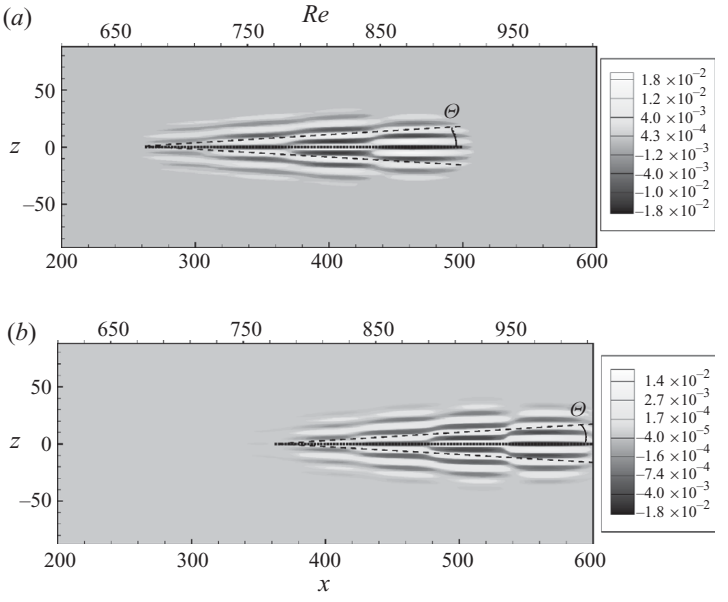

FIGURE 18. Contours of the streamwise component of the near-optimal perturbation for $\beta_L = 0.035$ on the plane $y = 1$, at $t = 0$ (a) and its linear evolution at $t = T_{max}$ (b).

the initial energy level. This could be the signal of the emergence of a 'global mode' (Huerre & Monkewitz 1990).

To generalize the result to larger spanwise domain lengths, the nonlinear evolution of the 'near-optimal' wave packet, discussed in the previous section, is simulated using a computational domain with $L_z = 180$. The initial energy is $E_0 = 0.5$ so that the flow is found to experience transition. Figure 18(a) shows the perturbation on an x–z plane at $t = 0$, and the angle Θ in the figure is equal to that obtained in the optimal case ($\Theta_{opt} \approx 4.5°$). Figure 18($b$) displays a snapshot of the state at the target time, $T_{max} = 247$, obtained by solving the linearized Navier–Stokes equations, for later comparison. The wave packet is convected downstream without remarkable structural changes and the angle Θ is unchanged with respect to the initial time (figure 18a). Figure 19a provides the snapshot of the state at $t = 160$, obtained by direct numerical simulation. The perturbation is mostly convected downstream, while being amplified. Whereas the streamwise modulation of the packet is almost unaffected compared to the initial solution, the flow structure experiences spanwise diffusion. At $t = 220$ (figure 19b), the streaks partially merge, and two 'kinks' appear near the leading edge of the most amplified streak, affecting the streamwise modulation of the wave packet. To better analyse such a stage of breakdown, local views of the contours of the wall-normal, spanwise and streamwise perturbation velocity components are shown in figures 20(a), 20(b) and 20(c), respectively. Two kinks can be observed in the wall-normal and streamwise perturbation velocity components, alternated in the streamwise direction and symmetric with respect to the $z = 0$ axis. On the other hand, an array of spanwise-antisymmetric transversal velocity packets alternated in the longitudinal direction are observed in figure 20(b). Such patterns are similar to those observed in the case of quasi-varicose streak breakdown (see Brandt *et al.* 2004), likely to occur when a low-speed streak interacts with a high velocity one incoming in its front. In figure 20(c) it can be observed that the spanwise perturbations affect not only the streaks A and

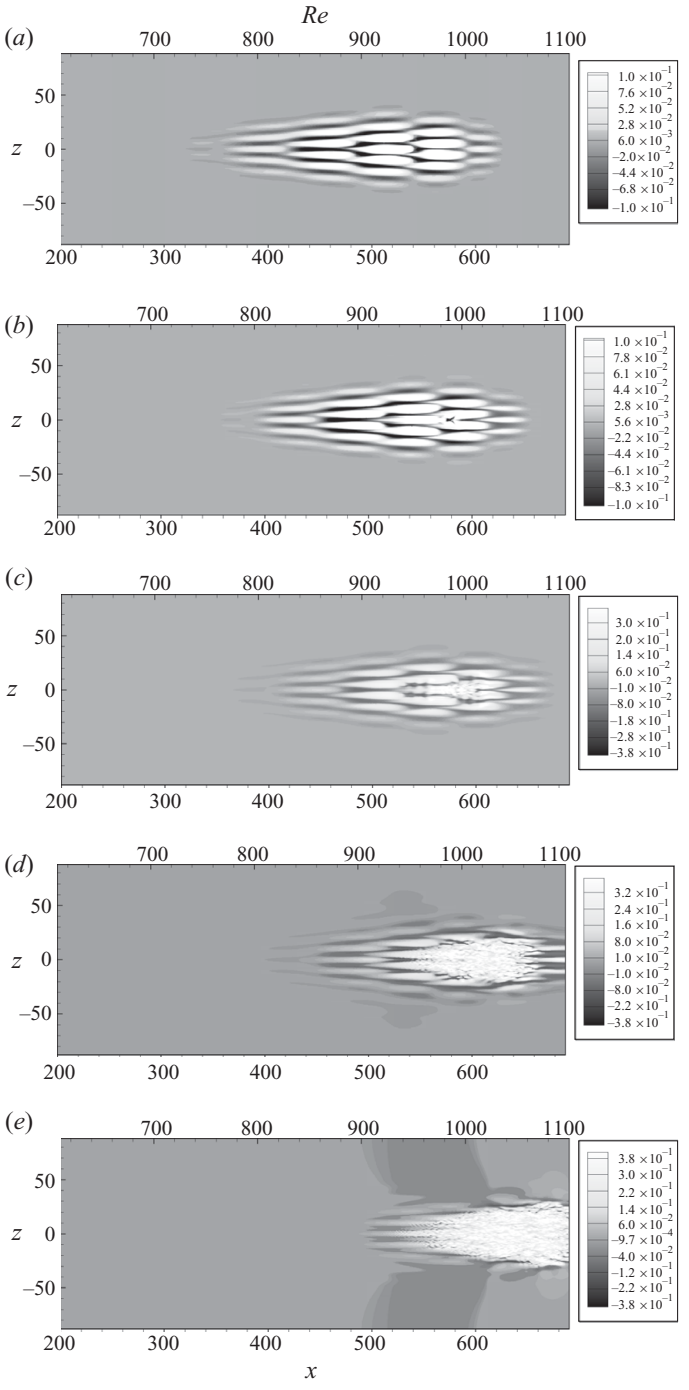

FIGURE 19. Contours of the streamwise component of the perturbation for $\beta_L = 0.035$ and $y = 1$, obtained by the direct numerical simulation at $t = 160$ (a), $t = 220$ (b), $t = 250$ (c), $t = 330$ (d) and $t = 420$ (e).

B on the $z = 0$ axis, but also the high-speed ones on the two sides of the $z = 0$ axis (labelled C and D). Indeed, the spanwise perturbations, although antisymmetric about the $z = 0$ axis, are almost symmetric with respect to the middle axis of C and D.

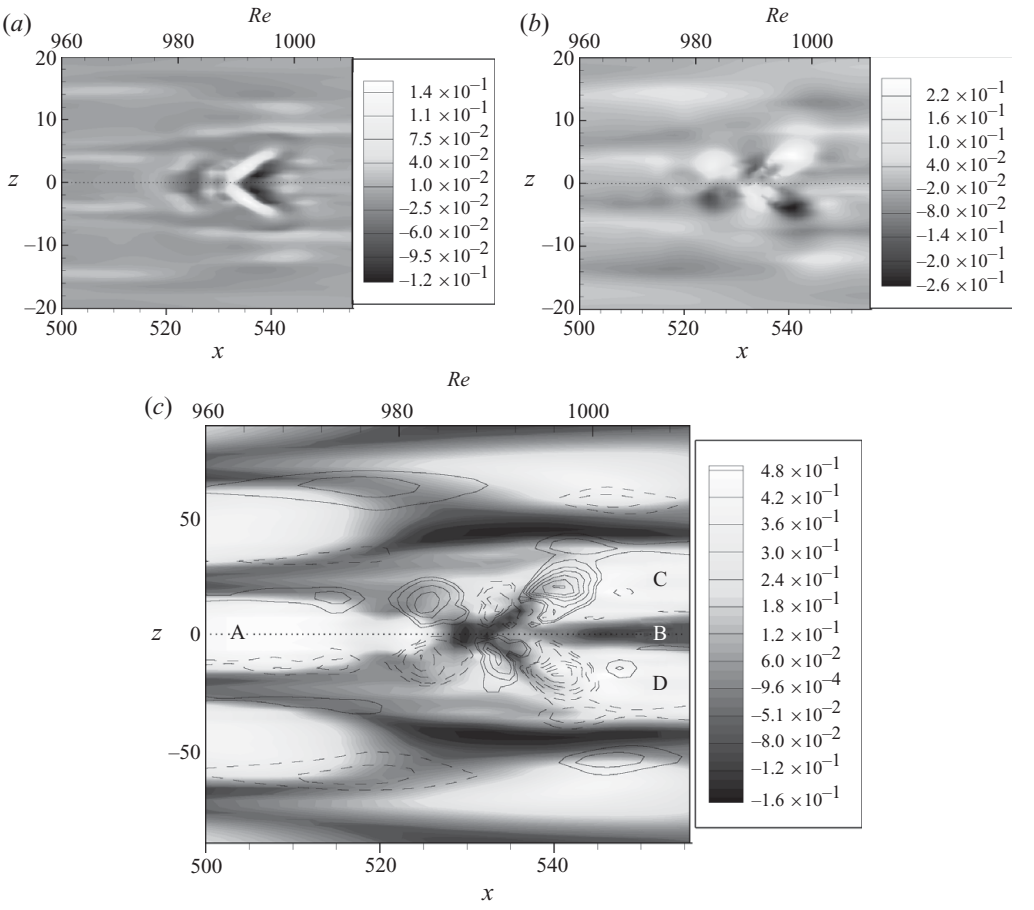

FIGURE 20. Contours of the wall-normal (a), spanwise (b) and streamwise (c) component of the perturbation for $\beta_L = 0.035$ and $y = 1$, at $t = 220$. The dotted line is the $z = 0$ axis, whereas solid and dashed lines in (c) represent the positive and negative spanwise component contours, respectively.

As a consequence, they induce spanwise oscillations on such streaks, resulting in a pattern which is typical of quasi-sinuous streak breakdown (cf. Brandt *et al.* 2004). Thus, it can be concluded that both the scenarios of quasi-sinuous and quasi-varicose breakdown can be identified in the present case because of the staggered arrangement of the streaks, so that both front and side interactions between fast and slow velocity regions take place simultaneously. Therefore, in the highly symmetric configuration examined here, four streaks break down simultaneously, explaining the effectiveness of the global optimal and near-optimal perturbations in inducing transition.

To better study the vortical structure in the interaction zone, the Q-criterion (Hunt, Wray & Moin 1988) is adopted, which consists in analysing the contours of the parameter:

$$Q = \tfrac{1}{2}(\|\boldsymbol{\Omega}\|^2 - \|\boldsymbol{S}\|^2), \tag{3.3}$$

$\boldsymbol{\Omega}$ and $\boldsymbol{S}$ being the vorticity tensor and the rate-of-strain tensor, respectively. Figure 21 shows that, before breakdown, a hairpin vortex is present in the interaction zone of the streaks labelled as A, B, C, and D, preceded upstream by a pair of quasi-streamwise vortices. At the interior of the hairpin, a low-momentum region is

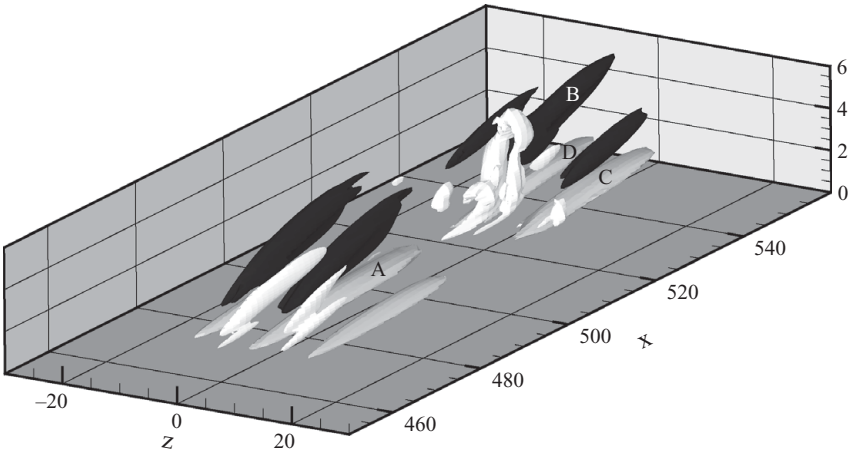

FIGURE 21. Iso-surfaces of the streamwise component of the perturbation (black surfaces represent negative perturbations, whereas dark grey ones indicate positive perturbations of absolute value equal to 0.5), and of the vortical structures identified by the Q-criterion (the light grey surfaces represent the positive value $Q = 660$). The perturbation has been extracted at $t = 180$.

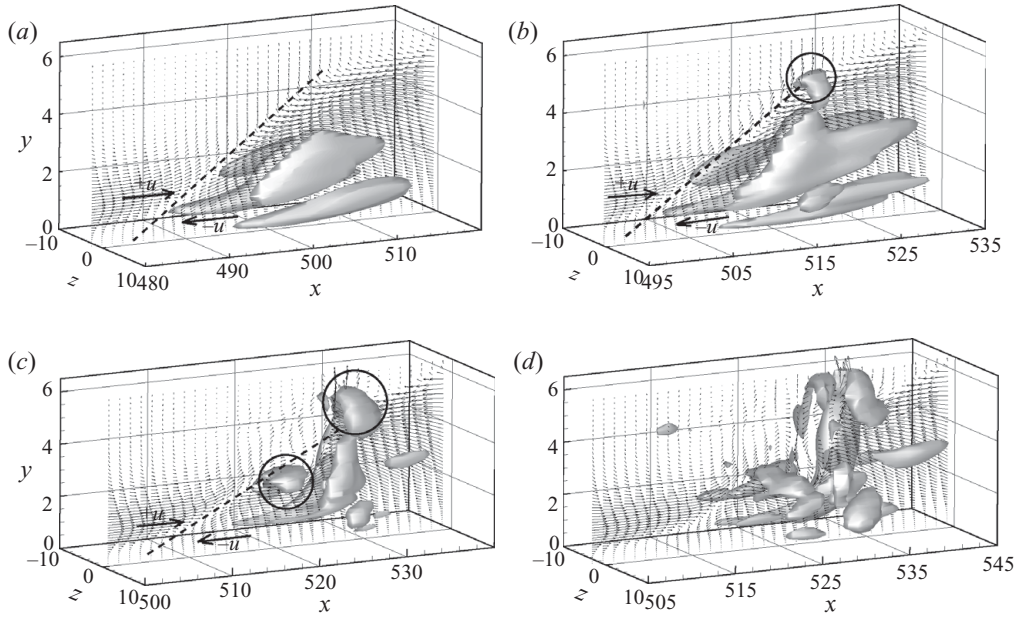

FIGURE 22. Iso-surfaces of the Q parameter and perturbation velocity vectors on the $z = 0$ plane at $t = 145$ (a), $t = 165$ (b), $t = 180$ (c) and $t = 190$ (d). The surfaces represent the positive values $Q = 370$ for (a) and (b) and $Q = 700$ for (c) and (d). The inclined shear layer is represented by the dashed line in (a–c).

found, corresponding to the low-speed streak B. This region tilts downstream, as also observed in the experiments by Lundell & Alfredsson (2004). To illustrate the mechanism of creation and breakdown of the hairpin vortex, the Q-contours identifying the hairpin vortex are plotted at four times, together with the velocity perturbation vectors on the x–y plane through its head. Figure 22(a) shows the

incipient hairpin at $t = 145$: two quasi-streamwise vortices, which are placed on the flanks of the low-speed streak, begin to increase their size in the wall-normal direction, due to the increasing downstream tilting of the low-momentum streamwise fluctuations. Ahead of such streamwise vortices, an inclined shear layer is produced, induced by the front interaction of the upstream high-speed streak with the downstream low-speed one. At time $t = 165$, due to the further increase (because of lift-up) of the low- and high-momentum perturbations, nonlinear effects allow the formation of a vortical region at the edge of the inclined shear layer, as shown in figure 22(b) by the black circle. Such a region of high spanwise vorticity generates an arch vortex connecting the two quasi-streamwise vortices, thus forming the head of the hairpin. At $t = 180$ (see figure 22c), this head is lifted from the wall, and a second arch vortex appears upstream of the first, along the inclined zone of interaction of the low- and high-speed streaks (shown by the second black circle in the figure). Finally, at $t = 190$, the first hairpin vortex further increases in size, while breaking up into smaller coherent patches of vorticity, although remnants of the original structure are still visible (cf. figure 22d).

A similar mechanism of generation of packets of hairpins has been discussed by Adrian (2007) for the case of fully developed turbulent boundary layers; in particular, the self-generation of packets of hairpins in streamwise succession, with size increasing downstream, was reported. Evidence for the presence of hairpin vortices in transitional flows has been recently given by Wu & Moin (2009), which have attributed the generation of such structures to the presence of Λ-vortices excited by receptivity to free-stream turbulence. In the present computation, it appears that the front interaction of the low and high momentum streaks is the primary cause of the hairpin formation in the early stages of transition, whereas the subsequent induction of new hairpins is probably linked to the oscillations of the low-momentum fluid comprised between the legs of the hairpin.

Such a transition scenario is interesting because it somehow connects two opposite views of transition, namely that grounded on transient growth and secondary instability of the streaks (Schoppa & Hussain 2002; Brandt *et al.* 2004), and the other based on vortex regeneration (Adrian 2007). In fact, in previous studies of transitional boundary-layer flows under free-stream turbulence (Brandt *et al.* 2004), the presence of hairpin vortices was not observed, and the breakdown of the streaks was attributed to an instability of the inflectional velocity profiles due to the interaction of low and high-speed streaks.

Going back to the evolution in time of the perturbation, figure 19(c) shows the presence of several subharmonics in both the streamwise and spanwise direction. Indeed, due to streak breakdown, close to the linearly optimal time (at $t = 250$) the most amplified elongated structures in the middle of the wave packet have already experienced transition. Later, as shown in figure 19(d), the turbulent region spreads out in the spanwise and streamwise direction leading the nearest streaky structures to break up. Finally, at $t = 420$ (figure 19e), the linear wave packet has totally disappeared and the disturbance takes the form of a localized 'turbulent spot'. The spanwise rate of spread of the spot, defined as the angle at its virtual origin between its plane of symmetry and its mean boundary, is measured by using the criterion of the 2 % free-stream velocity magnitude proposed by Wygnanski *et al.* (1976). Such an angle is very close to that measured by Wygnanski *et al.* (1976) for a boundary-layer flow, namely about 9°. It is about twice the optimal inclination of the initial wave packet ($\Theta_{opt} = 4.5°$), showing that turbulence spreads out more quickly in the spanwise direction than in the streamwise one. Moreover, figure 19(e) shows the

presence of a 'calmed region' trailing behind the chaotic zone, which is a typical feature of a turbulent spot (Schubauer & Klebanoff 1955). Thus, the near-optimal wave packet computed by means of the three-dimensional direct-adjoint approach represents a linear precursor of a 'turbulent spot'. The size and position of a turbulent spot are usually chosen by receptivity, a process which in the present computations is bypassed by injecting on the base flow a localized disturbance of given energy resulting from an incomplete optimization procedure. For such a reason, no general conclusion about the streamwise position of turbulent spots in a real boundary-layer flow can be drawn from here. Nonetheless, it can be concluded that the transition mechanism investigated here represents one – among many – viable path of transition via localized disturbances.

4. Conclusions and outlook

In this work a new attempt has been made to identify initial disturbances capable to provoke breakdown to turbulence effectively in a boundary-layer flow over a flat plate. The aim has been to optimize not simply an initial state (at $x=0$ or $t=0$) characterized by a single wavenumber (in space) and/or frequency (in time), but a wave packet, localized in the streamwise and spanwise direction.

A direct-adjoint three-dimensional optimization procedure and a global eigenvalue analysis are employed to compute the spatially localized perturbation capable to cause the largest growth of the disturbance energy in a finite non-parallel flat-plate boundary layer. The optimal initial perturbation is characterized by a pair of streamwise-modulated counter-rotating vortices, tilted upstream, resulting at optimal time in streak-like structures alternated in the streamwise direction. This indicates that perturbations with non-zero streamwise wavenumber have a role in the transient dynamics of a boundary layer. A scaling law is provided describing the variation of the streamwise modulation of the optimal initial perturbation with the streamwise domain length and the Reynolds number. Since the domain is homogeneous in the spanwise direction, the optimal initial perturbation is always characterized by a single wavenumber in this direction. Nevertheless, for sufficiently large domains it is unlikely that a single-spanwise wavenumber disturbance emerges in a boundary layer as a result of exogenous forcing. Thus, a near-optimal localized perturbation, characterized by a large spectrum of frequencies, has been extracted during the optimization process. Such a perturbation has the form of a wave packet with elongated disturbances modulated in the spanwise and streamwise directions. Notably, this near-optimal initial disturbance attains a gain which is less than 1 % smaller than the true optimal disturbance.

The capability of the localized optimal perturbations to induce transition has been investigated by means of direct numerical simulations. It is shown that the global optimal disturbance is able to induce transition for lower levels of the initial energy than local optimal and suboptimal perturbations. Interestingly, the local Reynolds number at which transition is initiated does not vary much with the initial energy level of the global optimal disturbance. Simulations are also performed for the nonlinear evolution of the near-optimal wave packet, which is found to evolve in a 'turbulent spot' spreading out in the boundary layer. Transition is initiated in a region of the flow close to the centre of the packet, by means of a mechanism including features of both quasi-sinuous and quasi-varicose breakdown. In fact, it is found that in this zone the streaks are able to interact on their sides as well as on their fronts, due to their alternated arrangement, so that more than one streak undergo transition at

the same time, explaining the efficiency of the optimal perturbation (as well as the near-optimal one) in yielding a chaotic behaviour. A hairpin vortex emerges in the region of interaction of the streaks prior to transition, generated by the inclined shear layer resulting from the front interaction of a low and a high-speed streak. Such an intense primary hairpin induces secondary hairpins and late stages of the breakdown see the continuous regeneration of such coherent structures.

The transition scenario presented here appears to connect two different views of transition: that based on transient growth and secondary instability of the streaks (Schoppa & Hussain 2002; Brandt *et al.* 2004) and the one describing breakdown via the continuous regeneration of vortices (Adrian 2007; Wu & Moin 2009). Although the present optimization is not capable to determine uniquely the position of a turbulent spot, an occurrence which depends on both receptivity and nonlinearity, the optimal and near-optimal wave packets computed by means of the three-dimensional direct-adjoint optimization represent a linear precursor of the spot, and the mechanism investigated here is a viable path to transition.

Current works is aimed at including the effects of nonlinearity in the optimization and at searching the localized perturbation able to lead the flow to turbulence most effectively.

This work was performed using HPC resources from GENCI-CCRT/IDRIS. The authors would like to thank R. Verzicco for providing the direct numerical simulation code, F. Alizard for providing the code for the global eigenvalue analysis, M. Napolitano for making possible the cooperation between the laboratories in which this work has been developed and C. Pringle for interesting discussions. This research has been supported by MIUR and Politecnico di Bari under contracts CofinLab2000 and PRIN2007.

Appendix. Numerical methods

In this section the numerical methods employed for the integration of the direct and adjoint equations and of the global eigenvalue problem are described. The performance of such methods are discussed as well.

Both linearized and nonlinear Navier–Stokes equations are integrated by a fractional step method using a staggered grid (Verzicco & Orlandi 1996). The viscous terms are discretized in time using an implicit Crank–Nicolson scheme, whereas an explicit third-order-accurate Runge–Kutta scheme is employed for the nonlinear terms. A second-order-accurate centred space discretization is used. The same approach is employed for the integration of the adjoint operator (2.4).

For the solution of the linearized Navier–Stokes equations, a fringe region of length $L_f = 90$ is adopted when using the reference domain ($L_x = 400$, $L_y = 20$, $L_z = 10.5$), whereas, for different domain lengths, the dimension of the fringe region is scaled proportionally to L_x. The forcing function applied in the fringe region is defined as

$$f = \begin{cases} \dfrac{A}{1 + \mathrm{e}^{\left(\frac{x_1 - x_{out}}{x - x_{out}} - \frac{x_1 - x_{out}}{x_1 - x}\right)}} & \text{for } x_{out} < x < x_1, \\ A & \text{for } x_1 < x < x_2, \\ \dfrac{A}{1 + \mathrm{e}^{\left(\frac{x_{out} + L_f - x_2}{x - x_2} - \frac{x_{out} + L_f - x_2}{x_{out} + L_f - x}\right)}} & \text{for } x_2 < x < x_{out} + L_f, \end{cases} \tag{A 1}$$

where x_1 and x_2 are placed at the abscissae $x_{out} + L_f/3$ and $x_{out} + 2L_f/3$, respectively, and $A = 100$. For the solution of the linearized Navier–Stokes equations, the reference

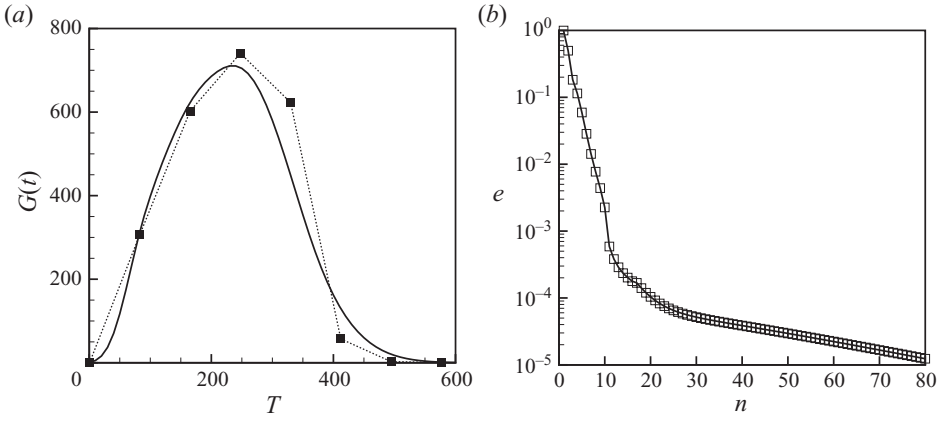

FIGURE 23. (*a*) Envelope of the optimal energy gain obtained by the direct-adjoint method (■) and by the global model (—); (*b*) normalized increment of the objective function e versus the number of iterations at $T = 247$, represented in a semilogarithmic scale.

computational domain is discretized by a $501 \times 150 \times 41$ Cartesian grid stretched in the wall-normal direction (the height of the first cell close to the wall is equal to 0.1, whereas the lengths of the cell in the x and z direction are 0.98 and 0.25, respectively). In order to ascertain that such a grid is sufficiently fine to accurately describe the linear dynamics of the considered flow, computations have been performed using a $801 \times 200 \times 61$ grid, and the results have been found to be essentially unchanged. Nonlinear simulations have been performed using a finer grid ($801 \times 200 \times 121$) chosen in order to resolve also the small scales of turbulence. Moreover, the streamwise length of the physical domain is increased to $L_x = 490$, to allow for a longer development of turbulent structures; this is achieved by replacing the fringe region with a non-reflecting convective boundary condition (Bottaro 1990). A longer domain can thus be studied at a reduced computational cost.

Concerning the global model, the problem (2.9) is discretized by a Chebyshev/Chebyshev collocation spectral method employing $N = 1100$ modes, and solved with a shift-and-invert Arnoldi algorithm using the ARPACK library (Lehoucq, Sorensen & Yang 1997), the residual being reduced to 10^{-12}. The modes are discretized using $n_x = 230$ collocation points in the x direction and $n_y = 47$ collocation points in the y direction. A study of the sensitivity of the global-model solution to the grid resolution and to the domain length has been carried out in Alizard & Robinet (2007).

The convergence properties of the algorithms are analysed computing a boundary-layer flow at $Re = 610$ using a domain with dimensions $L_x = 400$, $L_y = 20$, $L_z = 10.5$. The direct-adjoint optimization reaches a maximum value of the optimal energy gain, $G(t)$, of about 736 approximately at time $T_{max} \approx 247$ as shown in figure 23(*a*). Figure 23(*b*) provides the normalized increment of the objective function, $e = (E(T)^{(n)} - E(T)^{(n-1)})/E(T)^{(n)}$, versus the number of iterations, n, for a direct-adjoint computation performed at the optimal target time. The algorithm is able to reach very quickly a level of convergence of about 10^{-4}; then, the convergence rate decreases, so that about 80 iterations are needed to reach a level of convergence of 10^{-5}. Provided that only minor differences are observed between the solutions corresponding to the two convergence levels 10^{-4} and 10^{-5}, the convergence level 10^{-4} can be considered satisfactory. Concerning the computational cost of the direct-adjoint optimization, at the optimal target time, a convergence level of 10^{-4} is reached in about 8 h of CPU time on a single processor Intel(R) Core(TM) @ 2.67-GHz.

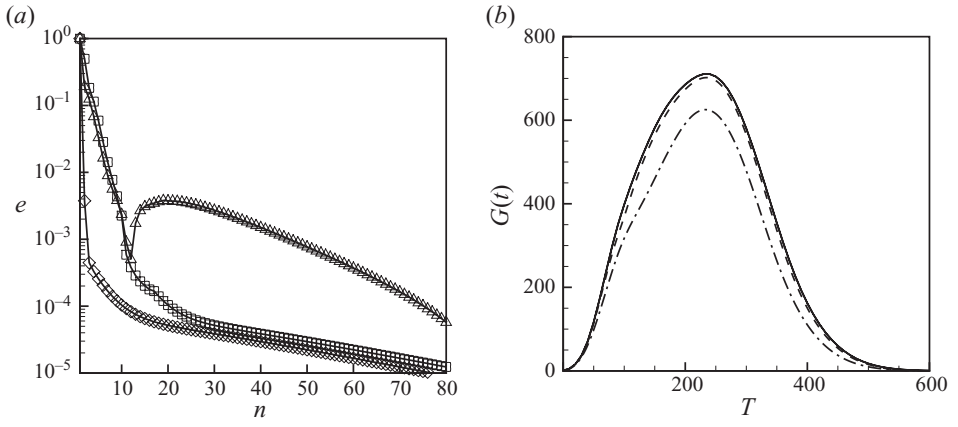

FIGURE 24. (*a*) Normalized increment of the objective function e versus the number of iterations at $T = 247$, represented in a semi-logarithmic scale for an initial guess resulting from: a direct-adjoint optimization stopped at the level of convergence $e = 10^{-3}$ (◆); the global model optimization (□); the global model optimization with a random noise of amplitude 10^{-8} superposed at the inlet points (△). (*b*) Envelope of the optimal energy gain obtained by the global model for $N = 1100$ (—), $N = 1000$ (— — —) and $N = 900$ (— · — · —) at $Re = 610$ and $L_x = 400$.

It is worth to point out that the iterative optimization technique is equivalent to perform power iterations for the maximization of a Rayleigh quotient, a procedure which is guaranteed to converge to the global optimum. The convergence history depends slightly on the initial guess, as shown in figure 24(*a*) which provides the normalized increment of the objective function, e, versus the number of iterations for an initial guess resulting from: (i) the direct-adjoint optimization stopped at the level of convergence $e = 10^{-3}$ (diamonds); (ii) the global model optimization (squares); (iii) the global model optimization with a random noise of amplitude 10^{-8} superposed at the inlet points (triangles). It is observed that, although the convergence is accelerated for an initial guess extracted from a previous direct-adjoint optimization, the slope of the convergence curve slightly varies. Moreover, when the initial guess is perturbed with some noise, although the normalized increment, e, temporarily increases, a rapidly decreasing curve is quickly re-established. A study of the convergence history is carried out also with respect to the time step chosen for the computation: the convergence curves are found to be independent of such a parameter.

To validate the results of the direct-adjoint method, the optimal energy gain is computed also by the global model of § 2.3. The resulting curve follows qualitatively the data obtained by the direct-adjoint method, although the maximum $G(t)$ is lower than that previously computed, and is equal to 710 at $t = 235$, as shown in figure 23(*a*) (solid line). Such a small discrepancy might be due to the different outflow boundary conditions employed in the two approaches. Another possible reason is that the continuous spectrum is captured only in a discrete sense by the present procedure. Hence it becomes important to employ both a large value of L_y (together with acceptable resolution along y) while including the largest possible number N of modes. For the solution of (2.11) and (2.9), $N = 1100$ modes have been employed which is the maximum allowed by the available memory allocation capacity for the storage of the matrices. To verify that $N = 1100$ is sufficient, the convergence of the global model optimization has been studied by varying the number of modes chosen for the optimization. Figure 24(*b*) shows the optimal energy gain curves computed

with $N = 900$ (dashed-dotted line), $N = 1000$ (dashed line) and $N = 1100$ modes (solid line). Although for the two most accurate computations the energy gain curves change only slightly, the convergence is not yet perfect. Concerning the computational cost, with $N = 1100$ modes, about 70 h are needed to compute the global spectrum using the eight cores of two Intel Itanium 2 Quad core @ 667 MHz processors. Once the spectrum is computed, such a method can quickly determine the energy gain curve with a high resolution in time; for example, 3 h are needed using a single core of an Intel Itanium 2 @ 667 MHz processor to compute the energy gain curve with a time increment of 10 in the interval 0–600. The same task takes about 500 h when using the direct-adjoint optimization. Thus, it is possible to conclude that the global model yields an acceptable estimate of the time at which the energy peaks; from this point on it is better to adopt the direct-adjoint procedure to evaluate accurately the maximum gain by performing the optimization in a small window around the optimal time obtained by the global model.

REFERENCES

Adrian, R. J. 2007 Hairpin vortex organization in wall turbulence. *Phys. Fluids* **19**, 041301.

Alizard, F. & Robinet, J.-C. 2007 Spatially convective global modes in a boundary layer. *Phys. Fluids* **19**, 114105.

Andersson, P., Brandt, L., Bottaro, A. & Henningson, D. S. 2001 On the breakdown of boundary layer streaks. *J. Fluid Mech.* **428**, 29–60.

Bakchinov, A. A., Grek, G. R. & Kozlov, V. V. 1992 A mechanism of turbulent spot formation. *Sibirskii Fiz.-Tekh. Z.* **4**, 39–45.

Barrow, J., Barnes, F. H., Ross, M. A. S. & Hayes, S. T. 1984 The structure of a turbulent spot in a Blasius flow. *J. Fluid Mech.* **149**, 319–337.

Bers, A. 1983 Space-time evolution of plasma instabilities – absolute and convective. In *Handbook of Plasma Physics* (ed. M. N. Rosenbluth & R. Z. Sagdeev) vol. 1, pp. 451–517. North-Holland.

Biau, D. & Bottaro, A. 2009 An optimal path to transition in a duct. *Phil. Trans. R. Soc.* A **367**, 529–544.

Biau, D., Soueid, H. & Bottaro, A. 2008 Transition to turbulence in duct flow. *J. Fluid Mech.* **596**, 133–142.

Bottaro, A. 1990 Note on open boundary conditions for elliptic flows. *Numer. Heat Trans.* B **18**, 243–256.

Brandt, L., Schlatter, P. & Henningson, D. S. 2004 Transition in a boundary layers subject to free-stream turbulence. *J. Fluid Mech.* **517**, 167–198.

Breuer, K. S., Cohen, J. & Haritonidis, J. H. 1997 The late stages of transition induced by a low-amplitude wavepacket in a laminar boundary layer. *J. Fluid Mech.* **340**, 395–411.

Breuer, K. S. & Landahl, M. T. 1990 The evolution of a localized disturbance in a laminar boundary layer. Part 2. Strong disturbances. *J. Fluid Mech.* **220**, 595–621.

Briggs, R. J. 1964 *Electron-Stream Interaction with Plasma*. MIT Press.

Butler, K. M. & Farrell, B. F. 1992 Three-dimensional optimal perturbations in viscous shear flow. *Phys. Fluids* A **4**, 1637–1650.

Chambers, F. W. & Thomas, S. W. 1983 Turbulent spots, wave packets and growth. *Phys. Fluids* **26**, 1160–1162.

Cohen, J., Breuer, K. S. & Haritonidis, J. H. 1991 On the evolution of a wave packet in a laminar boundary layer. *J. Fluid Mech.* **225**, 575–606.

Corbett, P. & Bottaro, A. 2000 Optimal perturbations for boundary layers subject to streamwise pressure gradient. *Phys. Fluids* **12**, 120–130.

Emmons, H. W. 1951 The laminar-turbulent transition in a boundary layer. Part I. *J. Aeronaut. Sci.* **18**, 490–498.

Faisst, H. & Eckhardt, B. 2003 Travelling waves in pipe flow. *Phys. Rev. Lett.* **91**, 224502.

Farrell, B. 1988 Optimal excitation of perturbations in viscous shear flow. *Phys. Fluids* **31**, 2093–2102.

Gad-el Hak, M., Blackwelder, R. F. & Riley, J. J. 1981 On the growth of turbulent regions in laminar boundary layers. *J. Aeronaut. Sci.* **110**, 73–95.

Gaster, M. & Grant, I. 1975 An experimental investigation on the formation and development of a wave packet in a laminar boundary layer. *Proc. R. Soc. Lond. Ser.* A **347**, 253–269.

Head, M. R. & Bandyopadhyay, P. 1981 New aspects of turbulent structure. *J. Fluid Mech.* **107**, 297–337.

Henningson, D. S., Lundbladh, A. & Johansson, A. V. 1993 A mechanism for bypass transition from localized disturbances in wall-bounded shear flows. *J. Fluid Mech.* **250**, 169–207.

Henningson, D. S., Spalart, P. & Kim, J. 1987 Numerical simulations of turbulent spots in plane Poiseuille and boundary-layer flows. *Phys. Fluids* **30**, 2914–2917.

Huerre, P. & Monkewitz, P. A. 1990 Local and global instabilities in spatially developing flows. *Annu. Rev. Fluid Mech.* **22**, 473–537.

Hunt, J. C. R., Wray, A. & Moin, P. 1988 Eddies, stream, and convergence zones in turbulent flows. *Tech. Rep.* CTR-S88. The Centre for Turbulence Research.

Landahl, M. T. 1980 A note on an algebraic instability of inviscid parallel shear flows. *J. Fluid Mech.* **98**, 243–251.

Landahl, M.T. 1990 On sublayer streaks. *J. Fluid Mech.* **212**, 593–614.

Lehoucq, R., Sorensen, D. & Yang, C. 1997 *ARPACK Users' Guide: Solution of Large Scale Eigenvalue Problems with Implicitly Restarted Arnoldi Methods*. SIAM.

Luchini, P. 2000 Reynolds number indipendent instability of the Blasius boundary layer over a flat surface: optimal perturbations. *J. Fluid Mech.* **404**, 289–309.

Lundbladh, A. & Johansson, A. V. 1991 Direct simulation of turbulent spots in plane Couette flow. *J. Fluid Mech.* **229**, 499–516.

Lundell, F. & Alfredsson, P. H. 2004 Streamwise scaling of streaks in laminar boundary layers subjected to free-stream turbulence. *Phys. Fluids* **16**, 1814–1817.

Marusic, I. 2009 Unravelling turbulence near walls. *J. Fluid Mech.* **630**, 1–4.

Matsubara, M. & Alfredsson, P. H. 2001 Disturbance growth in boundary layers subjected to free-stream turbulence. *J. Fluid Mech.* **430**, 149–168.

Orr, W. M. F. 1907 The stability or instability of the steady motions of a liquid. Part I. *Proc. R. Ir. Acad.* A **27**, 9–68.

Perry, A. E., Lim, T. T. & Teh, E. W. 1981 A visual study of turbulent spots. *J. Fluid Mech.* **104**, 387–405.

Sankaran, R., Sokolov, M. & Antonia, R. A. 1988 Substructures in a turbulent spot. *J. Fluid Mech.* **197**, 389–414.

Schmid, P. J. 2000 Linear stability theory and by pass transition in shear flows. *Phys. Plasmas* **7**, 1788–1794.

Schmid, P. & Henningson, D. 2001 *Stability and Transition in Shear Fows*. Springer.

Schoppa, W. & Hussain, F. 2002 Coherent structure generation in near-wall turbulence. *J. Fluid Mech.* **453**, 57–108.

Schubauer, G. B. & Klebanoff, P. S. 1955 Contributions on the mechanics of boundary layer transition. *Tech. Rep.* TN 3498. NACA.

Singer, B.A. 1996 Characteristics of a young turbulent spot. *Phys. Fluids* **8**, 509–512.

Sommerfeld, A. 1908 Ein Beitrag zur hydrodynamische Erklärung der turbulenten Flüssigkeitsbewegungen. In *Proceedings of the 4th International Congress of Mathematicians, III*. Rome, Italy, pp. 116–124.

Verzicco, R. & Orlandi, P. 1996 A finite-difference scheme for the three-dimensional incompressible flows in cylindrical coordinates. *J. Comput. Phys.* **123** (2), 402–414.

Wedin, H. & Kerswell, R. R. 2004 Exact coherent structures in pipe flow: travelling wave solutions. *J. Fluid Mech.* **508**, 333–371.

Wu, X. & Moin, P. 2009 Direct numerical simulation of turbulence in a nominally-zero-pressure-gradient flat-plate boundary layer. *J. Fluid Mech.* **630**, 5–41.

Wygnanski, I., Sokolov, M. & Friedman, D. 1976 On a turbulent spot in a laminar boundary layer. *J. Fluid Mech.* **78**, 785–819.

Zuccher, S., Luchini, P. & Bottaro, A. 2004 Algebraic growth in a Blasius boundary layer: optimal and robust control by mean suction in the nonlinear regime. *Eur. J. Mech.* B/*Fluids* **513**, 135–160.